ARTICLE

Hydroxylated sphingolipid biosynthesis regulates photoreceptor apical domain morphogenesis

Sarita Hebbar ®, Kai Schuhmann ®, Andrej Shevchenko ®, and Elisabeth Knust ®

Apical domains of epithelial cells often undergo dramatic changes during morphogenesis to form specialized structures, such as microvilli. Here, we addressed the role of lipids during morphogenesis of the rhabdomere, the microvilli-based photosensitive organelle of *Drosophila* photoreceptor cells. Shotgun lipidomics analysis performed on mutant alleles of the polarity regulator *crumbs,* exhibiting varying rhabdomeric growth defects, revealed a correlation between increased abundance of hydroxylated sphingolipids and abnormal rhabdomeric growth. This could be attributed to an up-regulation of *fatty acid hydroxylase* transcription. Indeed, direct genetic perturbation of the hydroxylated sphingolipid metabolism modulated rhabdomere growth in a *crumbs* mutant background. One of the pathways targeted by sphingolipid metabolism turned out to be the secretory route of newly synthesized Rhodopsin, a major rhabdomeric protein. In particular, altered biosynthesis of hydroxylated sphingolipids impaired apical trafficking via Rab11, and thus apical membrane growth. The intersection of lipid metabolic pathways with apical domain growth provides a new facet to our understanding of apical growth during morphogenesis.

Introduction

A characteristic hallmark of epithelial cells is the subdivision of their plasma membrane into an apical, a lateral, and a basal domain. The apical plasma membrane domain is often expanded and highly differentiated to execute specific functions, for example to increase absorption or to form the outer segment in vertebrate photoreceptor cells (PRCs), thus enhancing vision. Development of the apical membrane includes its specification, differentiation of cell type–specific specialized structures, and growth to achieve the mature size and shape.

To date, we have a good understanding of the molecular players (genes and protein complexes) and some of the underlying principles that regulate the primary polarization of the plasma membrane in different epithelial tissues (Riga et al., 2020; Rodriguez-Boulan and Macara, 2014). However, once specified, how does the apical membrane achieve its mature size and highly stereotyped shape? The formation of specialized structures, such as microvilli, appears to be largely driven by the underlying cytoskeleton, i.e., by the actin network, including ezrin/radixin/moesin proteins and binding partners (Apodaca, 2018; Fath and Burgess, 1995; Morales et al., 2004; Pelaseyed and Bretscher, 2018; Saotome et al., 2004; Sauvanet et al., 2015). Increase in length of microvilli in the apical stereocilia of sensory cells requires the joint activity of motor protein (myosins)

and actin-bundling protein Epsin (Lelli et al., 2016). Recently Crb1, an evolutionary conserved apical determinant, was shown to participate, along with myosin 3b and Epsin, in the extension of actin-based protrusions of spinal neurons in zebrafish (Desban et al., 2019). Overexpression of *Drosophila crumbs* (*crb*) can lead to an expansion of apical membranes, whereas lowered levels can cause its reduction (Lattner et al., 2019; Muschalik and Knust, 2011; Myat and Andrew, 2002; Pellikka et al., 2002; Wodarz et al., 1995).

While many proteins are known to contribute to the growth of the apical domain, there is little appreciation of the role of other molecules and cellular processes, for example lipid metabolism or redox reactions, in this process. More specifically, how does the cell use lipids to regulate the development and growth of the apical domain? So far, phosphoinositides and their metabolites, such as phosphatidylinositol 4,5-bisphosphate and phosphatidylinositol (3,4,5)-trisphosphate, are the only well-studied signaling lipids in the context of apicobasal polarity (Gassama-Diagne et al., 2006; Martin-Belmonte et al., 2007; Medelnik et al., 2018; Raghu et al., 2012; Krahn, 2020). But these constitute only a small subset of lipid species in relation to the enormous diversity of lipids in cells. An early lipidomics study on Madin–Darby canine kidney (MDCK) cells in culture revealed

that polarization of epithelial cells is coupled with major changes in the lipidome (Sampaio et al., 2011), but the mechanisms required to coordinate/integrate the multiple pathways regulated by an altered lipidome were not further analyzed.

Here, we addressed the role of lipids in apical membrane growth using *Drosophila melanogaster* PRCs. During pupal development, these cells develop a prominent apical domain, the rhabdomere, formed by ~40,000 closely packed microvilli (Cagan and Ready, 1989; schematized in Fig. 1 A). In the second half of pupal development, the original rudimentary microvilli increase in number and length and become more ordered (Longley and Ready, 1995). This growth is achieved in part by regulators of F-actin, a major structural component of the rhabdomere (Arikawa et al., 1990). Perturbation of the assembly of F-actin or its interaction with moesin results in early defects in the formation of the rudimentary microvilli (Baumann, 2004; Karagiosis and Ready, 2004; Pham et al., 2008; Zelhof and Hardy, 2004).

In addition, and somewhat unexpected, Rhodopsin, the light-sensing molecule, plays an important structural role in rhabdomere morphogenesis (Kumar and Ready, 1995). Biosynthesis of opsin (the protein moiety of Rhodopsin) is initiated in the last quarter of pupal development, followed by its apically directed transport toward the growing rhabdomere, and coincides with dramatic growth of the rhabdomere. Altered levels of Rhodopsin in the rhabdomere during this phase (Kumar and Ready, 1995), as well as improper trafficking (Beronja et al., 2005; Laffafian and Tepass, 2019; Satoh et al., 2005, 2015), impairs rhabdomere morphogenesis. Apart from Rhodopsin 1 (Rh1) and actin regulators, *Drosophila crb* also plays a role in rhabdomere growth. Mutants in *crb* exhibit abnormally shaped rhabdomeres, which fail to extend throughout the depth of the retina (Izaddoost et al., 2002; Johnson et al., 2002; Pellikka et al., 2002). Despite the fact that a huge amount of membrane is required to generate the rhabdomere, information about the role of lipids in this process are lacking. So far, studies on lipids in the fly eye have concentrated on their role in phototransduction mostly in mature PRCs (Muñoz et al., 2013; Raghu et al., 2009; Randall et al., 2015), but how rhabdomere morphogenesis is coupled to lipids and their metabolism has not been addressed.

Here, we used shotgun lipidomics of mutant alleles of *crb* with altered rhabdomeric shapes to elucidate the link between lipid composition and apical plasma membrane differentiation and growth. This strategy led to the identification of hydroxylated sphingolipids as influential players in rhabdomere morphogenesis. Furthermore, it revealed a novel role of hydroxylated sphingolipids in the regulation of apically directed delivery of Rhodopsin and hence in the growth of the rhabdomeres.

Results

crb is required for an extension of the rhabdomere along the proximodistal axis in the last quarter of development

Mutations in *crumbs* (*crb*) have been shown to affect rhabdomeric growth, resulting in bulky rhabdomeres (Izaddoost et al., 2002; Johnson et al., 2002; Pellikka et al., 2002). To better underst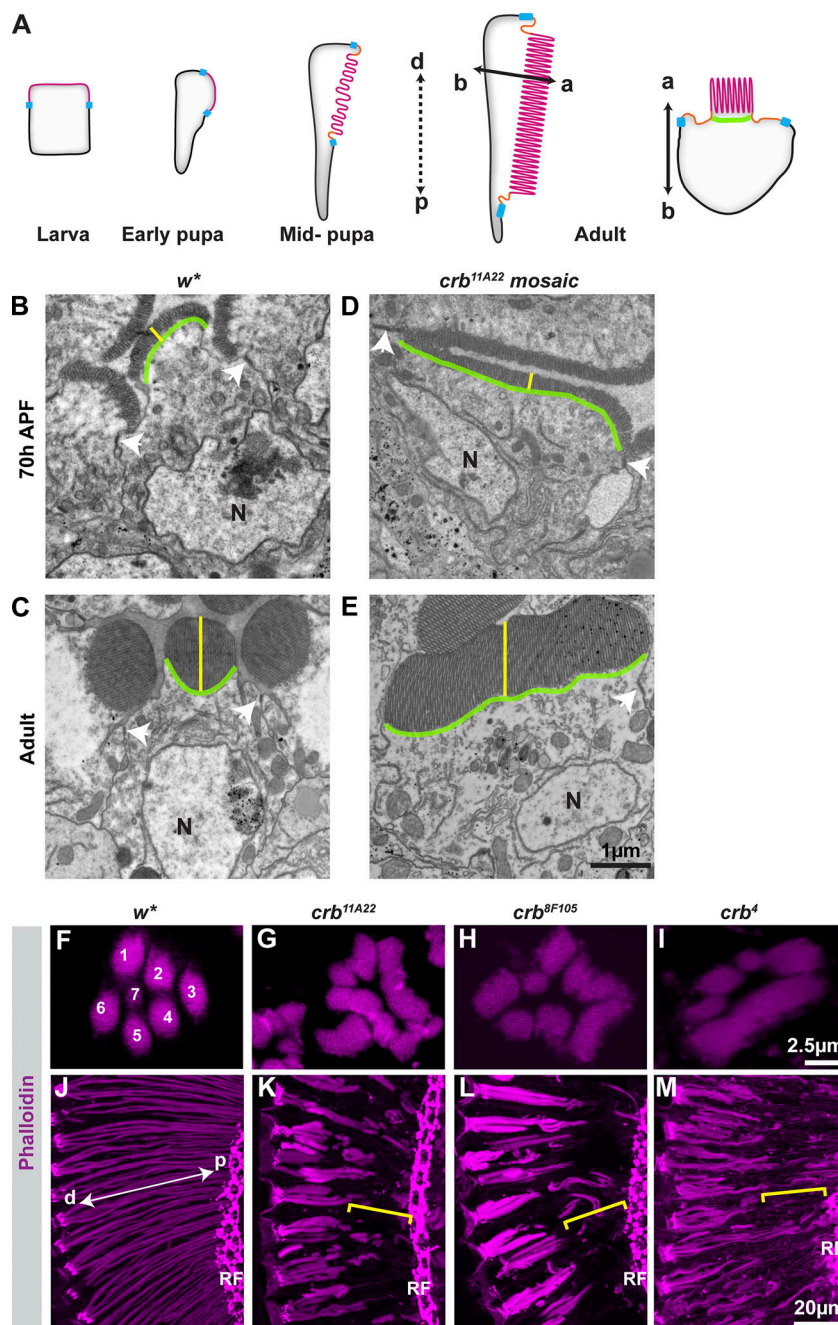and the basis of this phenotype, we compared the different aspects of rhabdomere growth in *crb* mutant and wild-type PRCs. The complex geometry of rhabdomeres is the combined consequence of growth in three dimensions that are temporally separated. (a) The base/width of the rhabdomere is established in midpupal phase concomitant with the stalk membrane (Fig. 1, B and C; and Fig. S1, D–F′; marked by green lines). (b) The thickness of the rhabdomere is the result of an increase in microvillar length along the apicobasal axis (Fig. 1, B and C; and Fig. S1, D–F′, yellow lines). (c) The extension of the rhabdomere along the proximodistal axis of the retina is due to an increase in number of microvilli (Figs. 1 A and S1, A–C). Any perturbation in PRC development in the last quarter of pupal development mainly affects extension and thickness of the rhabdomere and can be evaluated upon eclosion by staining with an F-actin marker.

In *crb* mutants, the width of the rhabdomeres in the distal end was increased already at midpupal stage (not depicted) and clearly visible 70 h after puparium formation (APF; compare Fig. 1, B and D, green lines). As in control PRCs, the width barely changed in *crb* mutants until adulthood (compare Fig. 1, D and E and B and C, green lines, respectively). During the growth phase, *crb* mutant rhabdomeres increased in thickness similarly to rhabdomeres of control PRCs (Fig. 1, D and E, yellow lines). However, the extension along the proximodistal axis was strongly affected (Fig. 1, K–M; Izaddoost et al., 2002; Johnson et al., 2002; Pellikka et al., 2002). This defect cannot be attributed to early defects in adherens junctions, since they recover during this phase (Pellikka et al., 2002; Tepass and Harris, 2007). It should be noted that this extension defect affects only the rhabdomere, but not the rest of the cell, which reaches the retinal floor. In summary, *crb* affects only two aspects of rhabdomeric growth: the width of the rhabdomere in the first half of pupal development, and the extension along the proximodistal axis in the second half of pupal development. The thickness of the rhabdomere was not affected. It should be noted that the width and the thickness of *crb* mutant rhabdomeres could be assessed only in the distal region due to the extension defects.

Hydroxylated sphingolipids are more abundant in *crumbs* mutant eyes

To identify lipids involved in rhabdomere morphogenesis, we conducted shotgun lipidomics of the eyes of four different *crb* alleles (*crb^{11A22}*, *crb^{8F105}*, *crb^4*, and *crb^{13A9}*) and compared them to two different genetic controls (*w** and wild type). While *crb^{11A22}*, *crb^{8F105}* (Jürgens et al., 1984; Wodarz et al., 1993), and *crb^4* (Pichaud and Desplan, 2001; Richardson and Pichaud, 2010) exhibit a reduced extension of the rhabdomeres as described above (compare Fig. 1 J with Fig. 1, K–M), *crb^{13A9}* does not show this developmental defect (Spannl et al., 2017). The inclusion of this allele in the lipidomics analyses provided a comprehensive toolkit of multiple alleles with distinct, characteristic phenotypes.

Lipidomic analyses included the absolute (molar) quantification of 174 lipid species, spanning 14 lipid classes (Data S1). The only clear and consistent change across *crb* mutants was an increase in the abundance of hydroxylated sphingolipids (Data S1),

Hebbar et al.
Hydroxylated sphingolipids in apical domain growth

Journal of Cell Biology   2 of 15
https://doi.org/10.1083/jcb.201911100

Figure 1. **Rhabdomere proximodistal extension is affected in *crumbs* mutants in the last quarter of pupal development. (A)** Cartoon (not drawn to scale) depicting the remodeling of an epithelial precursor cell from the larval imaginal disc to the mature adult photoreceptor (Cagan and Ready, 1989). The precursor is a simple epithelial cell with its apical domain (magenta), adherens junction (blue), and basal membrane (black). In the first day of pupal development (early pupa), the apical domain shifts to adopt a lateral position. In mid-pupal stages, the apical domain is subdivided into the stalk membrane (orange) and the incipient rhabdomere (magenta). Finally, in the second half of pupal development, the apical domain/rhabdomere grows tremendously by extending along its proximodistal (p-d) axis (black dashed double-headed arrow) and by increasing its thickness along the apicobasal (a-b) axis (black solid double-headed arrow) of the cell. The width in the rhabdomere in the adult (cartoon of a cross section) is highlighted by a light green curved line. **(B–E)** Electron micrographs of distal transverse sections of pupal eyes at 70 h APF (B and D) and adult eyes (C and E) showing rhabdomeres in control (*w**; B and C) and *crb*[11A22] mutants (D and E). N indicates the nucleus of the cells, and white arrowheads point to the adherens junctions, which are evident in wild-type and mutant cells at both time points. Yellow solid lines indicate rhabdomere thickness along the apicobasal axis of the cell. Green curved lines demarcate the rhabdomere width. Note that the width in the mutant is already affected at 70 h APF. Scale bar is indicated in E. **(F–I)** Optical sections from 12-µm-thick transverse sections at the distal end of adult eyes labeled with Alexa Fluor 555-Phalloidin to visualize F-actin. Seven PRCs (1–7) are evident. In three different *crb* mutant alleles (G–I), altered rhabdomeres are visible. At the distal end of PRCs, rhabdomeres are wider. **(J–M)** Projections of confocal stacks obtained from 12-µm-thick longitudinal sections of adult eyes labeled with Alexa Fluor 555-Phalloidin to visualize F-actin. White double-headed arrow indicates the p-d axis, with the lens to the left and the retinal floor (RF) to the right. Yellow brackets indicate the lack of rhabdomeric extension in *crb* mutant alleles. Scale bars are indicated in I and M.

particularly in ceramide phosphorylethanolamines (CerPE), the most abundant class of membrane sphingolipid in *Drosophila* (Carvalho et al., 2010, 2012; Guan et al., 2013), and in their precursors, the low-abundant ceramides (Cer). For example, a two-fold increase was observed for hydroxylated CerPE (ox-CerPE, Fig. 2 A). It should be noted that ox-CerPE represents only a minor (<10 mol%) fraction of the total CerPE class. Strikingly, the increase in the abundance of ox-CerPE was observed only in those *crb* alleles that exhibit improperly extended and bulky rhabdomeres (*crb*[11A22], *crb*[8F105], and *crb*[4]; Fig. 1, G–I). In contrast, *crb*[13A9] mutant retinas, which have normal-shaped rhabdomeres (Spannl et al., 2017), did not show any significant change in hydroxylated sphingolipid abundance (Fig. 2 A). Further analysis by higher collisional dissociation Fourier

transform (HCD FT) tandem mass spectrometry (MS/MS) fragmentation (Fig. S2) revealed that increased hydroxylation of sphingolipid species occurred at the fatty acid moieties. This increase is shown in Fig. 2 B for the most abundant sphingolipids, CerPE 34:1 and CerPE 36:1, bearing hydroxylated fatty acids (20:0:1 and 22:0:1). At the same time, we observed no changes in fatty acid hydroxylation in glycerophospholipid species. Therefore, we conclude that increased hydroxylation of long chain fatty acids in *crb* mutant retinas feeds into the sphingolipid biosynthetic pathway.

crumbs mutant eyes reveal increased *fa2h* transcription and oxidative stress signaling

This result raised the question as to the mechanisms by which *crb* regulates the abundance of hydroxylated sphingolipids.
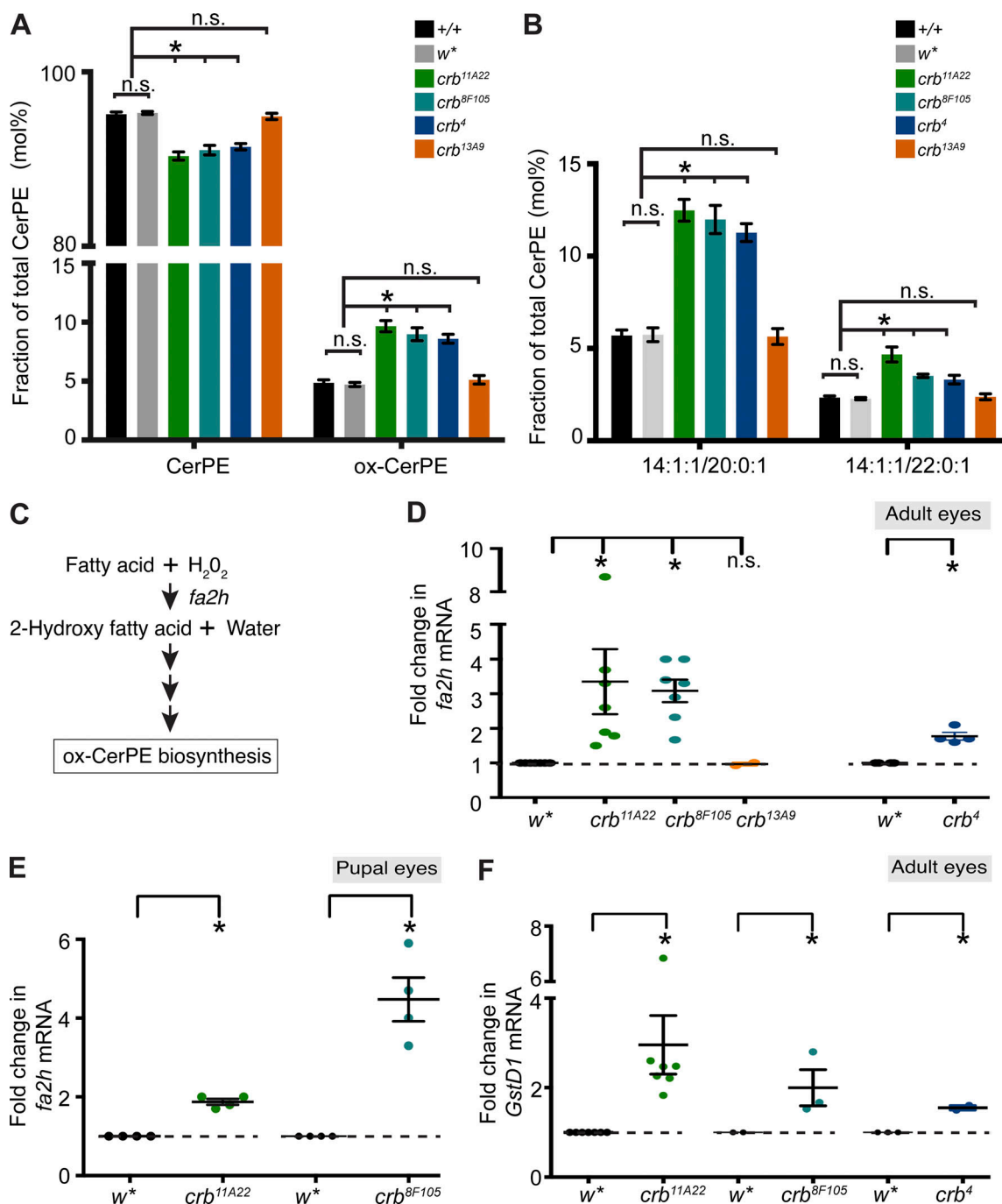
Figure 2. **crb mutant eyes have an altered lipidome and increased levels of fatty acid hydroxylase mRNA. (A)** Lipid distribution (denoted in mol%) within the sphingolipid class for nonhydroxylated CerPE and ox-CerPE, quantified by MS of eye extracts from controls (+/+ and w*), three crb mutants with bulky rhabdomeres (crb11A22, crb8F105, and crb4), and the crb allele crb13A9, which does not develop bulky rhabdomeres (Spannl et al., 2017). Bars represent mean ± SEM, and sample size = three biological replicates. Increased abundance of hydroxylated CerPE is observed only in crb mutants with bulky rhabdomeres. Statistical significance between groups is denoted by * (P < 0.05), whereas n.s. denotes no significant difference. **(B)** Lipid distribution (denoted in mol%) for major ox-CerPE species (14:1:1/20:0:1 and 14:1:1/22:0:1), with hydroxylation at fatty acid components identified and quantified by MS using MS^n fragmentation of lipids from eye extracts. Increased hydroxylation at the fatty acid moiety of the sphingolipids was observed in crb mutants with bulky rhabdomeres. Bars represent mean ± SEM, and sample size = three biological replicates. Statistical significance between groups is denoted by * (P < 0.05), whereas n.s. denotes no significant difference. **(C)** Part of the pathway proposed for the generation of sphingolipids hydroxylated at the fatty acid moiety, shown here for ox-CerPE. The process begins with the hydroxylation of the fatty acid by an enzyme encoded by fa2h (fatty acid (2) hydroxylase) in the presence of hydrogen peroxide. The hydroxylated fatty acid thus generated is included in the typical sphingolipid biosynthetic process to form the hydroxylated sphingolipid. **(D–F)** Comparison of mRNA levels by qRT-PCR for fa2h (D and E) and GstD1 (F) in adult (D and F) and pupal (60–80 h APF; E) eyes. Each replicate is shown as a dot, and lines represent mean ± SEM for fold-change in mRNA as indicated. Values are calculated after normalization with Gapdh1 mRNA and are relative to the control (w*; level indicated by black dotted line). *, statistical significance (P < 0.05); n.s., no significant difference between pairs as indicated by brackets.

Hydroxylated fatty acids are generated by fatty acid 2 hydroxy-lase (Fa2h, Fig. 2 C), encoded by *fa2h* in *Drosophila* (Carvalho et al., 2010). Therefore, we compared *fa2h* transcript levels in eyes dissected from mutant and control adult flies by real-time quantitative RT-PCR (real-time qRT-PCR). On average, a two- to fourfold increase in *fa2h* mRNA levels was observed in eyes of only those *crb* mutant alleles that develop bulky rhabdomeres (*crb*[IIA22], *crb*[8F105], and *crb*[4]), but not in *crb*[I3A9] mutant eyes (Fig. 2 D), which have normally organized rhabdomeres. The magnitude of increase of *fa2h* was not as high in *crb*[4] compared with the other two alleles (*crb*[IIA22] and *crb*[8F105]), which reflects the trend in ox-CerPE levels (Fig. 2 A). Interestingly, we already observed an increase in *fa2h* transcripts at pupal stages (60–80 h APF) of *crb*[IIA22] and *crb*[8F105] animals (Fig. 2 E). This period coincides with massive rhabdomere growth.

Hydroxylated fatty acids are lipid peroxidation products and are considered a metabolic outcome of the physiological stress response (Kaikkonen et al., 2004; Kuda et al., 2018). In fact, *fa2h* expression can be up-regulated under conditions of stress (Nagano et al., 2012). This is especially relevant because loss of *crb* leads to increased oxidative stress owing to an overactivation of NADPH oxidase, which is followed by increased levels of reactive oxygen species in adult mutant eyes (Chartier et al., 2012). We corroborated and extended these finding by showing that, as a consequence of increased reactive oxygen species levels, oxidative stress signaling was up-regulated in *crb* mutant eyes. As a marker for oxidative stress signaling, we used the expression of *GstD1*, a well-conserved oxidative stress response gene encoding a detoxification enzyme (Sawicki et al., 2003). We observed a significant increase in *GstD1* mRNA in adult eyes of *crb*[IIA22], *crb*[8F105], and *crb*[4] mutant flies (Fig. 2 F), which have improperly extended rhabdomeres. Increased oxidative stress signaling was further corroborated by the use of a transgenic reporter for oxidative stress signaling (*GstD-GFP*; Sykiotis and Bohmann, 2008) in adult eyes of *crb* mutants. In control eyes, GFP expressed from the reporter was observed in the pigment cells that envelop PRCs but was barely detectable in PRCs in the center of the ommatidium (Fig. S3, A and A′). In contrast, *crb* mutant retinas with improperly formed rhabdomeres exhibited increased oxidative stress signaling in PRCs, as revealed by increased GFP expression in the central part of the ommatidia (Fig. S3, B–C′).

Taken together, our data uncover a correlation between improperly formed rhabdomeres, increased oxidative stress signaling, and increased hydroxylated sphingolipids in *crb* mutant eyes. Increased levels of hydroxylated sphingolipids are due to an up-regulation of *fa2h* expression, which was particularly prominent at a stage of pupal development when rhabdomere growth takes place.

Perturbing the redox status of PRCs influences *fa2h* expression and rhabdomere extension

Given the coincidence between an altered redox state and impaired rhabdomere extension in *crb* mutants, we next asked whether altering the redox status of PRCs in an otherwise wild-type background affects rhabdomeric extension. To address this question, we genetically interfered with the quenching of superoxide radicals, known to contribute to an oxidizing environment. This can be done by manipulating the function of cytoplasmic Sod1 (Cu-Zn superoxide dismutase 1), which converts superoxide radicals into the less reactive molecule hydrogen peroxide. We reduced *Sod1* levels by RNAi expression (Missirlis et al., 2003) and used a heterozygous mutant allele (*Sod1*[n1]/+; Phillips et al., 1995), thereby increasing superoxide radicals. The mutant heterozygotes (*Sod1*[n1]/+) are associated with an increase in *GstD1* mRNA (Fig. 3 A), indicative of an altered redox state in these animals. This change was associated with increased levels of *fa2h* mRNA in *Sod1*[n1]/+ mutant heads (Fig. 3 B). Strikingly, eyes of heterozygous mutant flies (*Sod1*[n1]/+) and eyes with PRC-specific RNAi-mediated knockdown of *Sod1* were associated with abnormal rhabdomeres; they did not completely reach the base of the retina (Fig. 3, C′–E′). Thus far, we demonstrated that an altered redox status, achieved by reducing either *Sod1* or *crb*, which regulates the plasma membrane redox system (NADPH oxidase; Chartier et al., 2012), results in increased *fa2h* expression and induces defects in rhabdomere extension.

fa2h modulates rhabdomere growth

To further determine whether increased *fa2h* levels are the cause for defects in rhabdomere growth in *crb* mutants, we manipulated *fa2h* expression levels in wild-type and mutant retinas using *Rh1-Gal4*, which is active in the last quarter of pupal development, during which rhabdomeres grow tremendously. Neither overexpression (Fig. 4 B) nor knockdown of *fa2h* via RNA interference (Fig. 4 C) in an otherwise wild-type background induced any gross abnormalities in rhabdomere extension compared with control (Fig. 4 A). However, overexpression of *fa2h* in *crb*[IIA22] and *crb*[8F105] mutant retinas caused even more bulky and irregular rhabdomeres (compare Fig. 4, D and G, with Fig. 4, E and H, respectively, and Fig. 4 N for penetrance and quantitative comparisons). The lack of further enhancement of the *crb*[IIA22] phenotype of short rhabdomeres upon overexpression of *fa2h* (Fig. 4 N) is in agreement with earlier data showing that *crb*[IIA22] is a protein null allele, while some protein is still produced in *crb*[8F105] (Wodarz et al., 1993). In contrast, rhabdomeres appeared less bulky upon lowering *fa2h* levels by RNAi in a *crb* mutant retina (compare Fig. 4, D and G, with Fig. 4, F and I, respectively, and Fig. 4 N). The effectiveness of *fa2h* overexpression and knockdown on *fa2h* mRNA was confirmed by real-time qRT-PCR (Fig. 4 J). The rescuing effect obtained upon knockdown of *fa2h*, although not completely penetrant, was more pronounced in the *crb* allele with the weaker phenotype (*crb*[8F105]). Here, most of the rhabdomeres extended to the base of the retina (compare Fig. 4 I to respective controls in Fig. 4 G). The rescue of the extension defect was also obvious in cross sections (Fig. 4, K′–M′). In *crb*[8F105], fewer and/or thinner rhabdomeres were visible proximally (Fig. 4 L′). Upon knockdown of *fa2h* in this background, a full complement of seven rhabdomeres was clearly visible in the proximal region. Note that *fa2h* knockdown did not affect the enlarged width of the rhabdomeres distally. Overall, these results support the conclusion that defects in rhabdomere extension in *crb* mutant eyes are caused by increased *fa2h* expression.
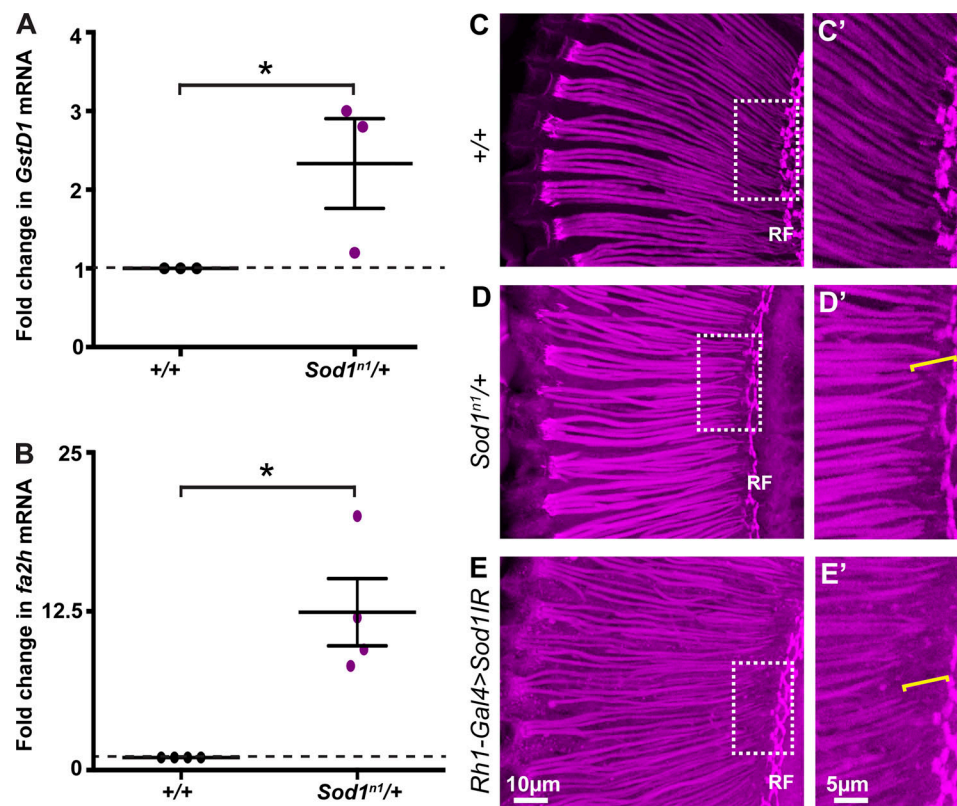
Figure 3. **Altered oxidative stress signaling is associated with increased *fatty acid hydroxylase* mRNA levels and improper rhabdomere extension.** **(A and B)** Comparison of mRNA (*GstD1*, A; *fa2h*, B) levels in wild-type (+/+) and *Sod1[n1]* heterozygous adult heads by real-time qRT-PCR. Each replicate is shown as a dot, and lines represent mean ± SEM for fold-change in mRNA as indicated. Values are calculated after normalization with *Gapdh1* mRNA and are relative to the control (+/+; level indicated by black dotted line). *, statistical significance ($P < 0.05$) between pairs as indicated by brackets. **(C–E)** Projections of confocal stacks obtained from 12-µm-thick longitudinal sections of adult eyes for genotypes indicated. Sections are labeled with Alexa Fluor 555-Phalloidin. Distal is to the left, proximal end with the retinal floor (RF) to the right. Scale bar is as indicated in E. **(C′–E′)** Digitally magnified areas as indicated by white dotted boxes in C–E, respectively, to show the incomplete extension of rhabdomeres in D′–E′ compared with C′. Scale bar is as indicated in E′.

Defects in rhabdomere growth are associated with reduced rhabdomeric Rh1

A major structural constituent of the rhabdomeric membrane of the outer PRCs (PRC 1–6) is the visual pigment Rh1. Rh1 is composed of the apoprotein opsin 1 (encoded by the gene *ninaE*), conjugated to the chromophore 3-hydroxy retinal, which is normally supplied by dietary carotenoids from plants (Isono et al., 1988). Defects in *ninaE* mutant retinas range from thinner rhabdomeres in hypomorphs to completely irregular microvillar structures in null mutants (Kumar and Ready, 1995). Rh1 was clearly observed in the rhabdomere of flies raised with normal food (Fig. 5, A and E). Reduction of the levels of the apoprotein opsin1, for example in the hypomorphic allele *ninaE[7]*, resulted in reduced Rh1 in the rhabdomeres (Fig. 5 C). A more detailed examination of the mutant phenotype revealed that these lowered rhabdomeric Rh1 levels coincided with impaired rhabdomere extension along the proximodistal axis (Fig. 5 D, bracket, vs. 5 B). Hence, reduction of Rh1 phenocopied the *crb* mutant rhabdomeric extension phenotype (Fig. 1, H–J).

Rhodopsin undergoes several steps of maturation, which take place during its trafficking through the secretory pathway. Absence of dietary carotenoid prevents maturation of opsin into Rhodopsin. As a consequence, most opsin accumulates in the perinuclear ER (Fig. 5 G; Ozaki et al., 1993; Satoh et al., 1997). In addition, the levels of Rhodopsin as well as rhabdomeric Rh1 (revealed by immuno-EM) are reduced (Huber et al., 1994; Sapp et al., 1991). We confirmed the development of thinner rhabdomeres (Lee et al., 1996) in wild-type PRCs upon carotenoid depletion (Fig. 5 G vs. 5 E). Strikingly, this treatment also prevents proper extension of rhabdomeres along the proximodistal axis, as many of them did not reach the retinal floor (Fig. 5, H and H′). This suggests that proper Rh1 levels in the rhabdomere are crucial for rhabdomeric growth, including its length and thickness. Accordingly, carotenoid depletion in *crb* mutants exacerbated the extension defects (Fig. 5 L vs. 5 J) and also affected the thickness of rhabdomeres (Fig. 5 K vs. 5 I). However, the increased width of *crb* mutant rhabdomeres at the distal end remained unchanged. This is not surprising, because rhabdomeric width is established at midpupal stages, before Rh1 expression. Overall, these results confirm that Rh1 in rhabdomeres is critical for rhabdomere proximodistal extension and thickness. They further suggested that impaired extension of rhabdomeres in *crb* mutants also depended on Rh1 levels. Given the observation that *fa2h* expression is enhanced in *crb* mutant retinas, this raises the question whether *fa2h* has an impact on Rhodopsin levels in the rhabdomere and/or its trafficking.
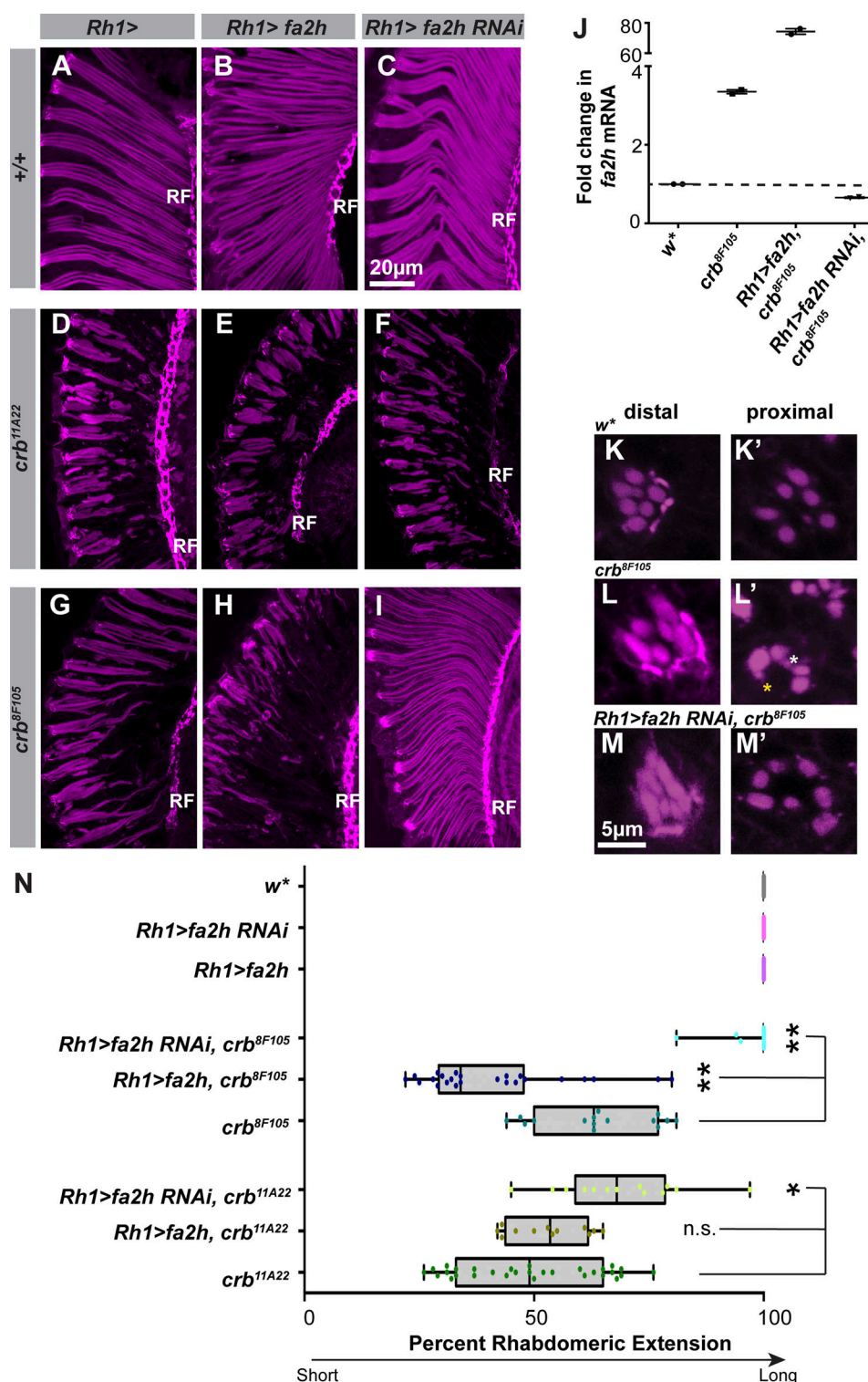
Figure 4. **Altering *fatty acid hydroxylase* levels in *crb* mutants modulates rhabdomere extension. (A–I)** Projections of confocal stacks obtained from 12-μm-thick longitudinal sections of fly heads labeled with Alexa Fluor 555-Phalloidin to visualize F-actin in rhabdomeres and the retinal floor (RF). Over-expression and RNAi-mediated knockdown specifically in the last quarter of metamorphosis is achieved with Rh1-Gal4 (Rh1>). In the sensitized background of *crb*^{11A22} (D–F) and *crb*^{8F105} (G–I), overexpression (*Rh1>fa2h*; E and H) and knockdown (*Rh1> fa2h RNAi*; F and I) of *fa2h* enhances (E and H) and decreases (F and I) the mutant phenotype of rhabdomere extension. The rescue upon *fa2h* RNAi overexpression is more complete in *crb*^{8F105}, where rhabdomeres appear leaner (I), as opposed to bulky rhabdomeres (G), and reach the retinal floor. Rhabdomere morphology is not affected by overexpression (B) or knockdown (C) of *fa2h* in a control (+/+) background. Scale bar is as indicated in C. **(J)** Comparison of mRNA levels in adult eyes by real-time qRT-PCR. Each replicate is shown as a dot, and lines represent mean ± SEM for fold-change in mRNA as indicated. Values are calculated after normalization with *Gapdh1* mRNA and are relative to the control (*w**; level indicated by black dotted line). **(K–M′)** Representative examples of optical sections of rhabdomeres from distal (K–M) and proximal (K′–M′) regions from 12-μm-thick transverse sections of the retina, labeled with Phalloidin (magenta). In the distal regions, the rhabdomeres appear wider in *crb*^{8F105} (L), and

upon knockdown of *fa2h* (M). Proximally, the extension defect in *crb*[8F105] (L′) is evident as smaller (white asterisk) or absent rhabdomeres (yellow asterisk). These defects are rescued upon knocking down *fa2h* in this genetic background (M′). **(N)** Box plot showing the range of rhabdomeric extension within each group (sample size of at least three eyes) for each genotype. 100 = full extension to the retinal floor. Each replicate is indicated by a dot, and the minimum and maximum values are indicated by the whiskers of the boxplot. n.s., not significant; ** (P < 0.001) and * (P < 0.05) indicate significant differences between population medians (brackets).

Increased *fa2h* levels limit Rh1 delivery to rhabdomeres

Besides improperly expanded and bulky rhabdomeres, punctate cytoplasmic accumulation of Rh1 is another feature of the *crb* mutant phenotype (Pocha et al., 2011), pointing to impaired Rh1 trafficking. As recently shown, absolute levels of opsin do not change in *crb* mutants with bulky rhabdomeres (Raghuraman et al., 2020). To further understand whether up-regulated *fa2h* impacts Rh1 distribution as well, we analyzed the localization of Rh1 by immunostaining. At steady state, Rh1 antibody labeled rhabdomeres and sub-rhabdomeric punctae in *crb* mutant (Fig. S4, A′ and D). Upon *fa2h* overexpression in *crb*[8F105] mutant PRCs, decreased rhabdomeric Rh1 staining and more Rh1-positive intracellular punctae (Fig. S4, B′ and E) were observed. The opposite effect on Rh1 distribution and rhabdomere shape was observed upon RNAi-mediated down-regulation of *fa2h* in mutant PRCs. Under this condition, most Rh1 staining was associated with rhabdomeres (Fig. S4, C′ and F). These images imply that Rh1 distribution is altered with changes in *fa2h*. Whether changes in *fa2h* levels impact Rh1 delivery and/or its stability cannot be concluded from these experiments.

Rhabdomere extension in the last quarter of metamorphosis coincides with a massive increase in the production of the apoprotein opsin, its maturation, and its trafficking as Rhodopsin through the secretory pathway to the rhabdomere via apically directed trafficking, mediated by the concerted action of Rab1, Syntaxin 5, Rab6, Rab11, Rip11, the exocyst complex, and MyoV (Beronja et al., 2005; Iwanami et al., 2016; Karagiosis and Ready, 2004; Laffafian and Tepass, 2019; Li et al., 2007; Pocha et al., 2011; Satoh et al., 2005). To follow the conversion of opsin and its trafficking as Rh1 to the rhabdomeres, the BLICS (blue light–induced chromophore supply) assay was used (Iwanami et al., 2016; Pocha et al., 2011; Satoh et al., 2005). Following carotenoid depletion, opsin was trapped primarily in the perinuclear ER of PRCs of adult flies (asterisk in Fig. 6 A) and was barely visible in the rhabdomeres. Only upon supplementation of the precursor (retinal) and its isomerization from all-trans retinal to 11-cis retinal via exposure to blue light, Rh1 was formed and trafficked to the rhabdomere (white arrowheads in Fig. 6, C and C′).

Based on BLICS assays, it has previously been shown that loss of *crb* affects Rh1 trafficking to the rhabdomere (Pocha et al., 2011). To explore whether increased levels of *fa2h*, associated with loss of *crb*, were responsible for this defect, we performed the BLICS assay in wild-type animals with increased levels of *fa2h*. At *t* = 0, we observed opsin accumulation in the ER similar to that in the control (asterisk in Fig. 6 B). However, after feeding retinal and at *t* = 180 min of exposure to blue light, very little Rh1 was detected in only few rhabdomeres, compared with control eyes (compare Fig. 6, D and D′, with Fig. 6, C and C′). This indicates that *fa2h* overexpression affects

conversion of opsin to Rh1 and/or trafficking through the secretory pathway.

We next sought to quantify the extent of Rh1 being delivered to the rhabdomeres. Hydroxylated fatty acid metabolism in worms has been shown to influence membrane trafficking mediated by the small GTPases, Rab11 and Rab7 (Li et al., 2018). In *Drosophila* PRCs, Rab11 colocalizes extensively to newly synthesized Rh1 following its exit from the Golgi and before being deposited in the rhabdomere. Indeed, *rab11* mutant rhabdomeres are smaller in size owing to a failure of Rh1 in reaching the rhabdomere (Satoh et al., 2005). On the other hand, Rab7 shows little overlap with Rh1 during the normal delivery of newly synthesized Rh1 to the rhabdomeres (Iwanami et al., 2016). We therefore quantified the overlap of Rh1- and Rab11-positive structures along the length of rhabdomeres from confocal images (Fig. S5, A–D) as a proxy/readout for the extent of Rh1 being delivered to rhabdomeres.

As previously published (Satoh et al., 2005), Rh1 overlapped with Rab11 upon release from ER in control retinas (Fig. 6, E–E″). In line with this, addition of carotenoids and exposure to blue light in BLICs assays resulted in a significant increase in Rh1 localized to Rab11-positive structures in control retinas (Fig. 6 G). In contrast, no increase in Rh1/Rab11 overlap was observed upon *fa2h* overexpression using the same conditions (Fig. 6 G). It should be noted that there were no significant changes in the overall level of opsin protein upon *fa2h* overexpression (Fig. S4 G), and the numbers of Rh1-positive and Rab11-positive structures were not altered (Fig. S5, E and F). From these results, it can be concluded that increased *fa2h* overexpression, also observed in *crb* mutants, impairs Rh1 trafficking to the rhabdomeres. In *crb* mutants, Rh1 localization in rhabdomeres decreased (Fig. S5 G; Pocha et al., 2011), and no change in Rh1/Rab11 overlap was revealed by BLICS assays (Fig. S5 H).

To summarize, increased *fa2h* expression, and thereby increased generation of hydroxylated sphingolipids (as observed, for example, in *crb* mutant PRCs), resulted in impaired Rh1 trafficking to the rhabdomeres and, as a consequence, to defective morphogenesis of rhabdomeres. These results highlight an as-yet-unknown role of hydroxylated sphingolipids in the growth of the apical domain of *Drosophila* PRCs during morphogenesis.

Discussion

Despite the importance of intact microvilli for the homeostasis of many epithelia, regulators controlling microvilli formation are only partially understood (Walton et al., 2018). Here, we used the rhabdomere of *Drosophila* PRCs, a highly expanded and elaborated apical membrane, as a model to dissect mechanisms
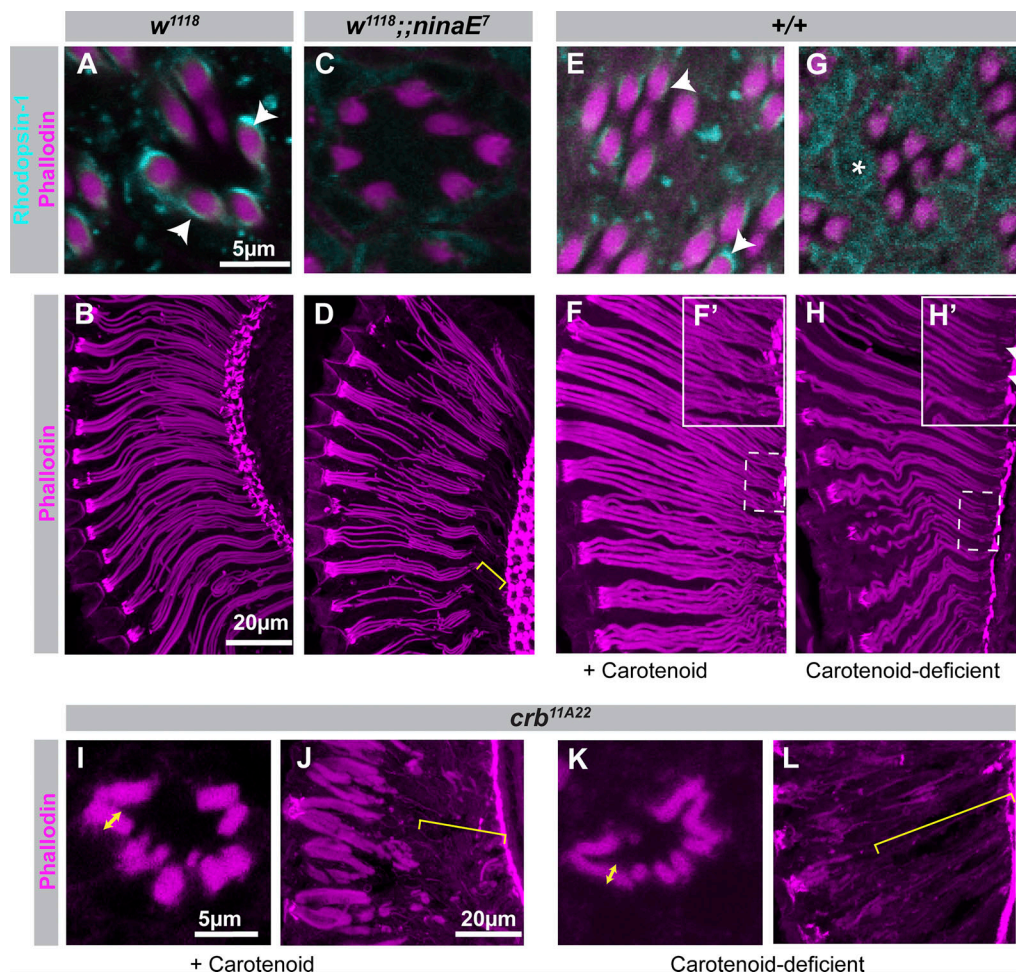
Figure 5. **Rhodopsin reduction results in abnormal rhabdomere extension. (A–D)** Representative images of optical sections (A and C) and projections (B and D) of 12-μm-thick transverse (A and C) and longitudinal (B and D) sections of control (A and B) and $ninaE^7$ (C and D) fly eyes, labeled with Alexa Fluor 555-Phalloidin (magenta; A–D) and an antibody against Rh1 (cyan; A and C). White arrowheads in A indicate Rh1 localized in a thin crescent in the inner rim of the rhabdomeres. Consistent with previous reports, Rh1 immunostaining does not fill the entire rhabdomere. This has been attributed to the inaccessibility of the antibody inside the tightly packed microvilli and light activation of phototransduction (Schopf et al., 2019). Rh1 staining is substantially reduced in rhabdomeres of mutant PRCs ($ninaE^7$, C). Yellow bracket in D denotes the incomplete extension of rhabdomeres of $ninaE^7$ mutant PRCs (D) compared with genetic control (B). **(E–H′)** Representative images of optical sections (E and G) and projections (F and H) of 12-μm-thick transverse (E and G) and longitudinal (F–H) sections of fly eyes (wild-type, +/+) raised on standard food (+ carotenoid, E and F) or carotenoid-depleted food (carotenoid deficient, G and H). F′ and H′ are digitally magnified images of the white dotted boxes indicated in F and H, respectively. Sections are labeled with Phalloidin (magenta; E–H) and an antibody against Rh1 (cyan; E and G). White arrowheads (E) indicate Rh1 in the thin crescent in the inner rim of the rhabdomeres. In rhabdomeres of flies raised in carotenoid-depleted food, Rh1 in the rhabdomere is substantially reduced, while opsin accumulates in the ER compartment surrounding the nucleus (asterisk). Note that rhabdomeres of flies raised on carotenoid-depleted food do not reach the retinal floor (white arrowhead in H′). Scale bar for transverse sections is as indicated in A and for longitudinal sections as indicated in B. **(I–L)** Representative images of optical sections (I and K) and projections (J and L) of 12-μm-thick distal transverse (I and K) and longitudinal (J and L) sections, prepared from crb^{11A22} mosaic eyes from flies raised on either standard food (+ carotenoid, I and J) or carotenoid-depleted food (carotenoid-deficient, K and L). Sections were labeled with Alexa Fluor 555-Phalloidin (magenta). Upon carotenoid depletion, rhabdomeres of crb mutant PRCs are not as thick (K) as those of flies raised on normal food (I); yellow double-headed arrows denote the thickness of the rhabdomere. Yellow brackets indicate incomplete extension of rhabdomeres along the proximodistal axis. Scale bar for transverse sections is as indicated in I and for longitudinal sections as indicated in J.

controlling the formation of microvilli. We show that increased transcription of *fa2h*, followed by increased levels of hydroxylated sphingolipids, is associated with defective rhabdomere morphogenesis. This is, at least partially, due to impaired apical trafficking of Rh1, an important structural component of the rhabdomeral membrane. These results also contribute to our understanding of the role of *crb* in rhabdomere morphogenesis. They imply that increased levels of hydroxylated sphingolipids particularly impact one aspect of rhabdomeral growth, namely

the addition of new microvilli, resulting in the extension of the rhabdomere along the proximodistal axis. Rhabdomeral thickness, determined by the length of the microvilli, is not obviously affected by changes in these lipids.

The connection between hydroxylated sphingolipid metabolism and apical domain morphogenesis is not unprecedented. Increased hydroxylation of sphingolipids was observed to be one of the major lipidomic changes during the polarization of MDCK cells (Sampaio et al., 2011), and inhibition of sphingolipid
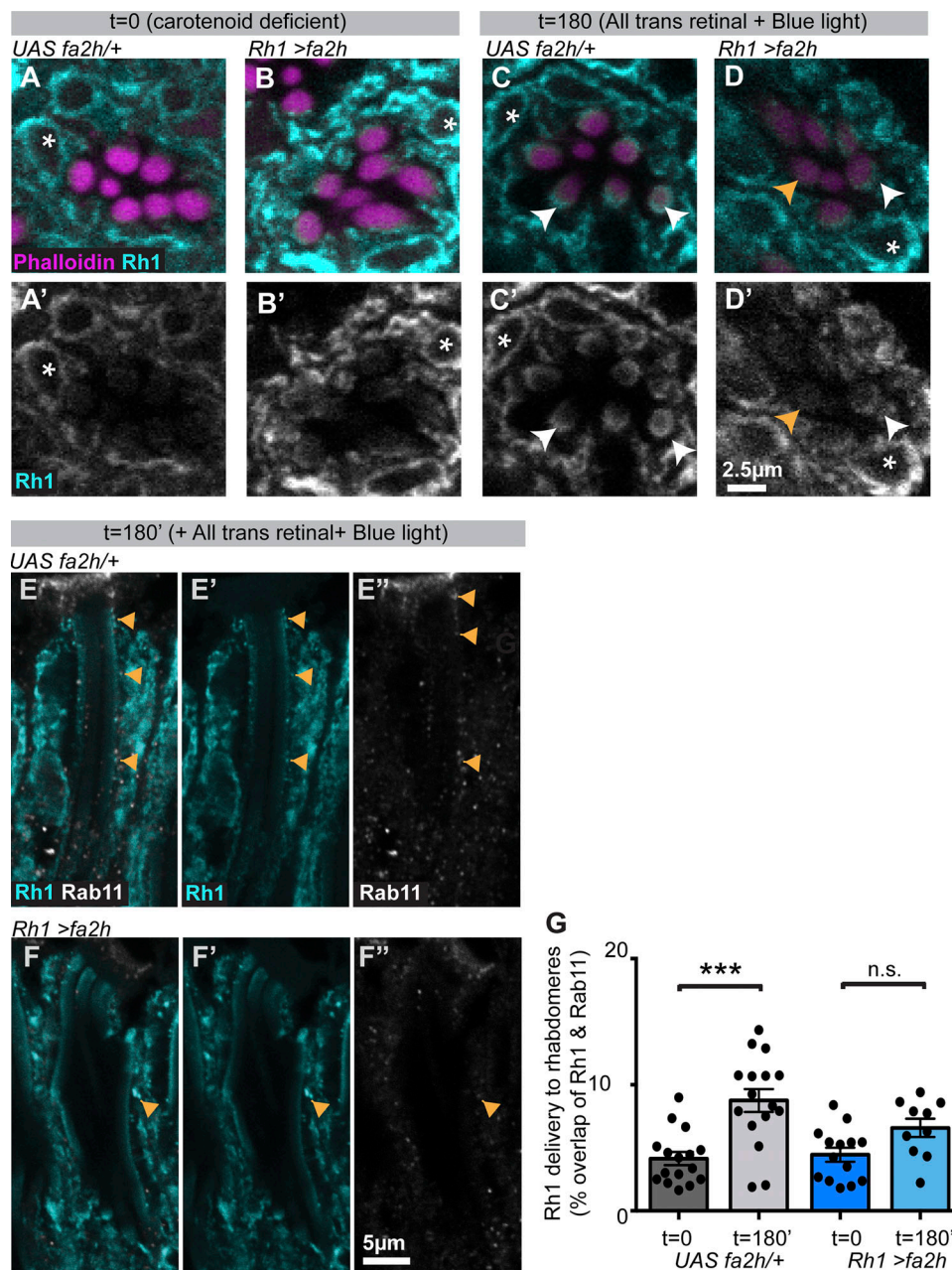
Figure 6. *fa2h* **overexpression results in reduced Rh1 in rhabdomeres. (A–D')** Images from BLICS assays. Representative images of optical cross sections of 12-μm-thick transverse sections of control eyes (*UAS fa2h/+*; A, A', C, and C') and eyes overexpressing *fa2h* (*Rh1>fa2h*; B, B', D, and D') double labeled with Alexa Fluor 555-Phalloidin (magenta) and an antibody against Rh1 (cyan). A'–D' are the Rh1/cyan channels from A–D, respectively. Images were taken from flies at *t* = 0 (before retinal supplementation; A–B') and *t* = 180 min (180') after exposure to blue light and with retinal supplementation (C–D'). In the absence of dietary carotenoids, opsin remains in the ER surrounding the nucleus (white asterisk). 180 min after BLICS, Rh1 is clearly visible in rhabdomeres in control eyes (white arrowhead, C–C'). Upon *fa2h* overexpression, some rhabdomeres have decreased Rh1 staining (orange arrowheads in D and D'). Scale bar is indicated in D'. **(E–F")** Representative images of optical slices from confocal stacks of 12-μm-thick longitudinal sections of control eyes (*UAS fa2h/+*; E–E") and eyes overexpressing *fa2h* (*Rh1>fa2h*; F–F") at *t* = 180' after exposure to blue light and with retinal supplementation. Sections are triple labeled with Alexa Fluor 555-Phalloidin (magenta, not shown here) and antibodies against Rh1 (cyan) and Rab11 (gray). Overlays of the cyan and gray channels are shown in E and F, whereas single-channel images for Rh1 and Rab11 are shown in E'/F' and E"/F", respectively. Rh1-positive structures that overlap with Rab11-positive structures are indicated with orange arrowheads in E–F". **(G)** Graph representing percentage overlap (mean ± SEM, at least three biological replicates) of sub-rhabdomeric Rh1- and Rab11-positive structures along the rhabdomere length obtained after applying BLICS assays (*t* = 0 and 180 min after blue light exposure and with retinal supplementation) in control retinas (*UAS fa2h/+*) and retinas after *fa2h* overexpression (*Rh1> fa2h*). The extent of Rh1 and Rab11 overlap is computed from confocal images of fly eye sections labeled with antibodies against Rh1 and Rab11 (examples provided in E–F"). Control eyes (gray) show a statistically significant increase in the extent of overlap in these two structures upon release of Rh1 trafficking (+ all trans retinal and blue light). In comparison, upon *fa2h* overexpression, there is no difference in extent of overlap between Rh1 and Rab11 upon release of Rh1 trafficking. n.s., no significant difference; ***, significant difference (P < 0.001).

Hebbar et al.
Hydroxylated sphingolipids in apical domain growth

Journal of Cell Biology   10 of 15
https://doi.org/10.1083/jcb.201911100

biosynthesis resulted in a reduced number of apical microvilli on their apical surface (Poole et al., 2004). Likewise, the *Caenorhabditis elegans* orthologue of *fa2h, fath-1,* was identified in a screen for genes affecting intestinal polarity (Zhang et al., 2011). Until now, however, the link between hydroxylated sphingolipids and their metabolism and polarization of epithelial cells was limited to circumstantial evidence. We now clearly demonstrate that manipulating hydroxylated sphingolipid metabolism, at least in a sensitized genetic background, is sufficient to modulate rhabdomere/apical domain extension.

How do hydroxylated sphingolipids and their metabolism affect rhabdomeric/apical domain growth? Given the low abundance of hydroxylated sphingolipids in the overall fly eye lipidome, we consider it unlikely that they play any major structural role in rhabdomere morphogenesis, e.g., by promoting the stability of Rhodopsin in the rhabdomeric membrane. We rather favor the conclusion that *fa2h* and thereby hydroxylated sphingolipids play a role as regulators of apical trafficking. This conclusion is based on two findings: (1) less newly synthesized Rh1 is delivered to the rhabdomeres upon overexpression of *fa2h,* as revealed by BLICS assays, which mimic Rh1 pulse-chase experiments; and (2) a similar defect in Rh1 trafficking has been observed in *crb* mutant PRCs (Pocha et al., 2011), which have increased levels of *fa2h* expression. In particular, we identified an effect on post-Golgi trafficking of Rh1 via the Rab11-mediated pathway. Accumulation of cytoplasmic vesicles is observed upon genetic perturbation of Rab11 and/or genes that encode for Rab11 interacting proteins (Li et al., 2007; Otsuka et al., 2019; Satoh et al., 2005). However, no obvious accumulation of similar vesicles was observed in *crb* mutant PRCs (not depicted). Thus, the trafficking defect observed upon *fa2h* overexpression cannot be attributed to a general increase/decrease in Rab11 compartments, but rather alludes to a defect in sorting apical cargo. These results are consistent with studies in *C. elegans,* where apical compartments labeled with Rab11 and Rab7 are affected upon loss of *fath-1* (Li et al., 2018).

Hydroxylated sphingolipids, as glycosphingolipids, are proposed to regulate the sorting of apically directed vesicles by combining different polarity cues (Zhang et al., 2011). In line with this, we propose that increased *fa2h* transcription (and hence an increase in hydroxylated sphingolipids) prevents apical membrane (rhabdomere) growth by inhibiting trafficking of Rh1 via the apical Rab11 compartments. By regulating the amount of Rh1 delivered to the rhabdomere, *fa2h* modulates the amount of rhabdomeric membrane in *Drosophila* PRCs, and hence has an impact on rhabdomere growth. Whether *fa2h* additionally promotes stability of Rhodopsin in the rhabdomeric membrane via the presence of more hydroxylated sphingolipids could not be addressed here. Interestingly, exogenously labeled hydroxylated fatty acids (the precursors of hydroxylated sphingolipids) preferentially distributed to apically localized membrane-bound compartments in the epithelial cells of the *C. elegans* gut (Li et al., 2018).

Unexpectedly, *fa2h* overexpression or knockdown in an otherwise wild-type background does not result in an obvious rhabdomeric extension phenotypes. This may be because Rh1 trafficking depends on the concerted action of Rab1, Rab6, Rab11,

Rip11, and MyoV as well as the Rab-effector proteins such as Parcas (Rab11GEF) and Rab11 interacting proteins such as dRip11 (Iwanami et al., 2016; Karagiosis and Ready, 2004; Li et al., 2007; Otsuka et al., 2019; Pocha et al., 2011; Satoh et al., 2005), and to the amount of F-actin (Pham et al., 2008). Although sphingolipids can induce changes in the cytoskeleton (Zeidan et al., 2008), we have not observed any overt changes in the staining of F-actin in the rhabdomere. Therefore, we speculate that increased *fa2h* acts to fine-tune growth by slowing down delivery of Rh1 and hence addition of new rhabdomeric membrane.

Yet, in a sensitized background, i.e., in cells homozygous mutant for *crb,* which have impaired Rh1 trafficking (Pocha et al., 2011) or upon carotenoid depletion, which also reduces Rh1 levels, *fa2h* overexpression now decreases Rh1 delivery via Rab11. Crb normally limits oxidative stress (Chartier et al., 2012), and the resulting oxidative status (low oxidative stress) normally limits *fa2h* expression. In *crb* mutants, however, an altered oxidative status (increased oxidative stress) causes an upregulation of *fa2h* transcription, which, in turn, results in severely reduced Rh1 delivery and improperly extended rhabdomeres. The *fa2h* dependence of rhabdomeric growth described here is only one aspect of the pleiotropic cellular response to an altered redox status of increased oxidative stress signaling due to loss of *crb.* Interestingly, loss of *crb* in epithelial cells of larval salivary glands impairs Rab6-, Rab11-, and Rab30-dependent apical trafficking and hence apical membrane homeostasis (Lattner et al., 2019). Whether this is also caused by increased oxidative stress and/or defects in sphingolipid metabolism remains to be analyzed.

In conclusion, this work elucidates an interplay between oxidative stress, lipid metabolism, and apical domain growth during PRC morphogenesis. It will be interesting to investigate whether this link between cell metabolism and apical membrane growth and morphogenesis is a more widespread phenomenon in epithelial biology.

Materials and methods

Fly stocks
Fly lines used in this study are documented in Table S1. Genotypes are listed in Table S2 for each figure. All fly crosses were maintained at 25°C under a standard 12-h light-dark cycle with a light intensity ranging from 600 to 1,000 lux. Unless specified, all flies were reared on a standard cornmeal-yeast–based diet.

Staging of pupae and adults
Pupae were collected at 0 h APF as white prepupae and placed on moistened filter paper discs in a Petri dish. They were allowed to age at 25°C until the desired age, and then the heads were dissected and processed as previously described (Spannl et al., 2017). Adults were collected within 0–6 h of eclosion and immediately processed as described (Spannl et al., 2017). Females were used in all experiments with adult flies except Western blotting.

BLICS assay
BLICS assays were done as described (Iwanami et al., 2016; Pocha et al., 2011; Satoh and Ready, 2005). Briefly, flies were

Hebbar et al.
Hydroxylated sphingolipids in apical domain growth

Journal of Cell Biology 11 of 15
https://doi.org/10.1083/jcb.201911100

reared on a carotenoid-depleted diet (Pocha et al., 2011). Adult flies were collected within 0–6 h after eclosion. Some flies were collected to prepare sections of eyes (carotenoid deficient), while others were transferred to vials containing carotenoid-free food supplemented with all trans-retinal (17.6 mM; Sigma-Aldrich; made in ethanol and allowed to crystalize on the surface). Flies were left in the dark for 48 h on this food. After this pre-incubation period, flies were exposed to blue light for 3 h. At this time point, heads were dissected and fixed with minimum exposure to white light.

Cryosectioning, immunostaining, and imaging
12-µm cryosections were obtained and immunostained as described previously (Spannl et al., 2017). Antibodies and fluorescently tagged dyes used are listed in Table S3. Samples were mounted in Vectashield (Vector Labs), and imaged with an Olympus FV1000 confocal microscope with a 60× Plan Apochromat oil objective (numerical aperture = 1.35) at ambient room temperature. Confocal z-stacks were obtained using an optical sectioning thickness of 0.33 or 1.0 µm.

Image processing and figure panel generation
Images were processed using Fiji (Schindelin et al., 2012) for making projections of the z-stacks and Adobe Photoshop CS5.1 for adjusting brightness and contrast. Adobe Illustrator CS3 was used for image assembly.

The percentage extension of the rhabdomere along the proximodistal axis (Fig. 4 N) was calculated as a ratio of the length of the rhabdomere (measured from projections in Fiji from rhabdomere cap to its most proximal part) to the retinal length (measured from projections in Fiji from rhabdomeric cap to the retinal floor). Sample sizes comprised at least three regions of interest (ROIs) from retinal sections of three to five eyes (biological replicates).

For quantification of Rh1- and Rab11-positive punctae, the entire z-stack from longitudinal sections was used, and an ROI of fixed size that comprised the length of three to four ommatidia was selected using the phalloidin channel as reference. Rh1-positive regions and Rab-11 positive regions were segmented for the whole stack. Using Fiji (Schindelin et al., 2012), a spot colocalization plugin, ComDet, was used as in Freal et al. (2019) for this ROI across the whole stack. This plugin provided the number of Rh1- and Rab11-positive structures and overlap (expressed as percentage overlap) of Rh1-positive and Rab11-positive structures for each slice in the z-stack of the ROI. A geometric mean of the various parameters across the z-stack constituted one biological replicate. Two to three ROIs from at least three eyes were used to compute mean ± SEM and make statistical comparisons.

Real-time qRT-PCR
qRT-PCR was performed as described (Spannl et al., 2017). Briefly, RNA extraction was performed using a standard Trizol-based (Invitrogen) procedure with phase separation using chloroform according to the manufacturer's instructions. Approximately 10 heads or 40–50 dissected eyes per genotype constituted one biological replicate, and at least two to five

biological replicates were used. cDNA generation was performed using SuperScript RT kit (Invitrogen) with a starting amount of 1 µg total RNA. qPCR was performed using primers described in Table S4.

Quantitative shotgun profiling of fly eyes lipidome
Fly eyes were dissected, pooled in groups of 10 in 200 µl isopropanol in 1.5-ml tubes (Eppendorf), and snap-frozen in liquid nitrogen. Sample size consisted of three biological replicates pooled from three to five independent crosses. Tissues were stored at –80°C. Before lipid extraction, samples were thawed and dried in a vacuum centrifuge for 30 min. 140 µl of water and a spatula of 1 mm zirconium beads (BioSpec) were added to the sample. Samples were then subjected to two cycles of bead beating (Qiagen TissueLyzer II) for 1.5 min at 30 Hz and 4°C.

To the homogenate were added 740 µl of a mixture of internal standards dissolved in methyl t-butyl ether/methanol (10:3; vol:vol). The aliquot of internal standards contained 539 pmol of Zymosterol D5, 73 pmol DG-D5 34:0, 138 pmol PC 25:0, 109 pmol LPC 13:0, 67 pmol PS 25:0, 147 pmol PE 25:0, 53 pmol LPE 13:0, 90 pmol PI 25:0, 68 pmol PG 25:0, 102 pmol Cer 30:1;1, and 74 pmol CerPE 29:1;1 (lipids purchased from Avanti Polar Lipids; see abbreviations in Table S5). The mixture was shaken for 2 h at 4°C and centrifuged for 5 min at 13,400 rpm and 4°C. The upper organic phase was collected into two glass vials and dried under vacuum. Before their analysis by MS, lipid extracts were dissolved in isopropanol/methanol/chloroform mixture (4:2:1; vol:vol:vol) with 7.5 mM ammonium formate (mix1) or methanol/chloroform mixture (5:1; vol:vol) with 0.1% trimethylamine (mix2). Shotgun lipidomics analyses were performed on a Q Exactive mass spectrometer (Thermo Fisher Scientific) equipped with a robotic nanoflow ion source TriVersa NanoMate (Advion BioSciences; Schuhmann et al., 2012) using the following acquisition methods: (a) samples dissolved in mix1: broadband FT MS$^+$ (range of m/z 350–1,100, target mass resolution $R_{m/z=200}$ = 140,000; automatic gain control (AGC) = 3×10^6) followed by targeted HCD FT MS/MS$^+$ (precursor isolation width = 1 Th; $R_{m/z=200}$ = 140,000, AGC = 2×10^4) under the normalized collision energy (NCE) of 20% and 35%; or (b) samples dissolved in mix1 and mix2: broadband FT MS$^-$ (range of m/z 400–1200, target mass resolution $R_{m/z=200}$ = 140,000, AGC = 3×10^6), followed by targeted HCD FT MS/MS$^-$ (precursor isolation width = 1 Th, $R_{m/z=200}$ = 140,000; AGC = 2×10^4) with NCE of 23% and 35%.

Lipid species were quantified by HCD FT MS/MS using LipidXplorer software (Herzog et al., 2011; Schuhmann et al., 2017). CerPE quantification relied on HCD FT MS/MS$^+$ at NCE 20% producing a lipid class–specific neutral loss fragment of $\Delta m/z$ = 141.0191 (see Fig. S2).

Western blotting
Five fly heads from each genotype were homogenized in 10 µl of 4× SDS-PAGE sample buffer (200 mM Tris-HCl, pH 6.8, 20% glycerol, 8% SDS, 0.04% bromophenol blue, and 400 mM DTT). After dilution with radioimmunoprecipitation assay buffer (150 mM sodium chloride, 1% Triton X-100, 0.5% sodium deoxycholate, 0.1% SDS, and 50 mM Tris, pH 8), lysates were

Hebbar et al.
Hydroxylated sphingolipids in apical domain growth

Journal of Cell Biology
https://doi.org/10.1083/jcb.201911100

12 of 15

heated at 37°C for 30 min. Lysates equivalent to 2.5 heads were loaded and run on a 15% acrylamide gel, and the proteins were transferred onto a membrane (Nitrocellulose Blotting Membrane 10600002; GE Healthcare Life Science). Primary antibodies were incubated overnight at 4°C and included anti-Rh1 (4C5; 1:500) from Developmental Studies Hybridoma Bank and anti-α-Tubulin (1:5,000) from Sigma-Aldrich. As secondary antibody, IRDye 800CW goat anti-mouse IgG (1:15,000; LI-COR Biotechnology) was used. The fluorescent signal from the dry membrane was measured using an Odyssey Sa Infrared Imaging System 9260-11P (LI-COR Biotechnology). The intensity of the bands was analyzed using Image Studio v4.0 software. The reported value was obtained following normalization of the intensity values for Rh1 with the corresponding Tubulin intensity values and the number of heads loaded onto the gel.

Statistical analyses

Statistical comparisons were performed in PrismPad software. Data distribution was assumed to be normal, but this was not formally tested. Statistical significance was determined by ANOVA followed by Tukey test for all comparisons across a set (e.g., lipidomics) or Bonferroni for specific pairwise comparisons (real-time qRT-PCR) with a confidence interval of 95%. When only two conditions were compared with each other, an unpaired, 2-tailed t test was used to determine significance with a confidence interval of 95%. For comparisons of rhabdomere extension, population medians between genotype pairs were compared using the Kolmogorov–Smirnov test with a confidence interval of 95%.

Abbreviations

Abbreviations are listed in Table S5.

Online supplemental material

Fig. S1 shows that the growth of rhabdomeres in the last quarter of pupal development is manifested by an extension and an increase in thickness. Fig. S2 shows the identification of CerPE species by FT MS and HCD FT MS/MS in positive ion mode. Fig. S3 shows the increased intensity of GstD-GFP reporter in *crb* mutant PRCs. Fig. S4 shows Rh1 localization at steady state. Fig. S5 shows Rh1-Rab11 overlap following BLICS assays. Table S1 describes fly lines. Table S2 lists genotypes. Table S3 lists chemical reagents and antibodies. Table S4 lists primers. Table S5 lists abbreviations. Data S1 contains the lipid species abundance (as mol%) across different alleles and controls (for each condition, there are at least n = 3 biological replicates) used in this study.

Acknowledgments

References

Apodaca, G. 2018. Role of Polarity Proteins in the Generation and Organization of Apical Surface Protrusions. *Cold Spring Harb. Perspect. Biol.* 10. a027813. https://doi.org/10.1101/cshperspect.a027813

Arikawa, K., J.L. Hicks, and D.S. Williams. 1990. Identification of actin filaments in the rhabdomeral microvilli of *Drosophila* photoreceptors. *J. Cell Biol.* 110:1993–1998. https://doi.org/10.1083/jcb.110.6.1993

Baumann, O. 2004. Spatial pattern of nonmuscle myosin-II distribution during the development of the *Drosophila* compound eye and implications for retinal morphogenesis. *Dev. Biol.* 269:519–533. https://doi.org/10.1016/j.ydbio.2004.01.047

Beronja, S., P. Laprise, O. Papoulas, M. Pellikka, J. Sisson, and U. Tepass. 2005. Essential function of Drosophila Sec6 in apical exocytosis of epithelial photoreceptor cells. *J. Cell Biol.* 169:635–646. https://doi.org/10.1083/jcb.200410081

Cagan, R.L., and D.F. Ready. 1989. The emergence of order in the Drosophila pupal retina. *Dev. Biol.* 136:346–362. https://doi.org/10.1016/0012-1606(89)90261-3

Carvalho, M., J.L. Sampaio, W. Palm, M. Brankatschk, S. Eaton, and A. Shevchenko. 2012. Effects of diet and development on the *Drosophila* lipidome. *Mol. Syst. Biol.* 8:600. https://doi.org/10.1038/msb.2012.29

Carvalho, M., D. Schwudke, J.L. Sampaio, W. Palm, I. Riezman, G. Dey, G.D. Gupta, S. Mayor, H. Riezman, A. Shevchenko, et al. 2010. Survival strategies of a sterol auxotroph. *Development.* 137:3675–3685. https://doi.org/10.1242/dev.044560

Chartier, F.J.-M., E.J.-L. Hardy, and P. Laprise. 2012. Crumbs limits oxidase-dependent signaling to maintain epithelial integrity and prevent photoreceptor cell death. *J. Cell Biol.* 198:991–998. https://doi.org/10.1083/jcb.201203083

Desban, L., A. Prendergast, J. Roussel, M. Rosello, D. Geny, C. Wyart, and P.L. Bardet. 2019. Regulation of the apical extension morphogenesis tunes the mechanosensory response of microvilliated neurons. *PLoS Biol.* 17. e3000235. https://doi.org/10.1371/journal.pbio.3000235

Fath, K.R., and D.R. Burgess. 1995. Microvillus assembly. Not actin alone. *Curr. Biol.* 5:591–593. https://doi.org/10.1016/S0960-9822(95)00117-5

Freal, A., D. Rai, R.P. Tas, X. Pan, E.A. Katrukha, D. van de Willige, R. Stucchi, A. Aher, C. Yang, A.F.M. Altelaar, et al. 2019. Feedback-Driven Assembly of the Axon Initial Segment. *Neuron.* 104:305–321.e308.

Gassama-Diagne, A., W. Yu, M. ter Beest, F. Martin-Belmonte, A. Kierbel, J. Engel, and K. Mostov. 2006. Phosphatidylinositol-3,4,5-trisphosphate

regulates the formation of the basolateral plasma membrane in epithelial cells. *Nat. Cell Biol.* 8:963–970. https://doi.org/10.1038/ncb1461

Guan, X.L., G. Cestra, G. Shui, A. Kuhrs, R.B. Schittenhelm, E. Hafen, F.G. van der Goot, C.C. Robinett, M. Gatti, M. Gonzalez-Gaitan, et al. 2013. Biochemical membrane lipidomics during *Drosophila* development. *Dev. Cell.* 24:98–111. https://doi.org/10.1016/j.devcel.2012.11.012

Herzog, R., D. Schwudke, K. Schuhmann, J.L. Sampaio, S.R. Bornstein, M. Schroeder, and A. Shevchenko. 2011. A novel informatics concept for high-throughput shotgun lipidomics based on the molecular fragmentation query language. *Genome Biol.* 12:R8. https://doi.org/10.1186/gb -2011-12-1-r8

Hu, Y., R. Sopko, M. Foos, C. Kelley, I. Flockhart, N. Ammeux, X. Wang, L. Perkins, N. Perrimon, and S.E. Mohr. 2013. FlyPrimerBank: an online database for Drosophila melanogaster gene expression analysis and knockdown evaluation of RNAi reagents. *G3 (Bethesda).* 3:1607–1616. https://doi.org/10.1534/g3.113.007021

Huber, A., U. Wolfrum, and R. Paulsen. 1994. Opsin maturation and targeting to rhabdomeral photoreceptor membranes requires the retinal chromophore. *Eur. J. Cell Biol.* 63:219–229.

Isono, K., T. Tanimura, Y. Oda, and Y. Tsukahara. 1988. Dependency on light and vitamin A derivatives of the biogenesis of 3-hydroxyretinal and visual pigment in the compound eyes of *Drosophila melanogaster*. *J. Gen. Physiol.* 92:587–600. https://doi.org/10.1085/jgp.92.5.587

Iwanami, N., Y. Nakamura, T. Satoh, Z. Liu, and A.K. Satoh. 2016. Rab6 Is Required for Multiple Apical Transport Pathways but Not the Basolateral Transport Pathway in *Drosophila* Photoreceptors. *PLoS Genet.* 12. e1005828. https://doi.org/10.1371/journal.pgen.1005828

Izaddoost, S., S.-C. Nam, M.A. Bhat, H.J. Bellen, and K.-W. Choi. 2002. *Drosophila* Crumbs is a positional cue in photoreceptor adherens junctions and rhabdomeres. *Nature.* 416:178–183. https://doi.org/10.1038/ nature720

Johnson, K., F. Grawe, N. Grzeschik, and E. Knust. 2002. *Drosophila* crumbs is required to inhibit light-induced photoreceptor degeneration. *Curr. Biol.* 12:1675–1680. https://doi.org/10.1016/S0960-9822(02)01180-6

Jürgens, G., E. Wieschaus, C. Nüsslein-Volhard, and H. Kluding. 1984. Mutations affecting the pattern of the larval cuticle in Drosophila melanogaster: II. Zygotic loci on the third chromosome. *Wilehm Roux Arch Dev Biol.* 193:283–295. https://doi.org/10.1007/BF00848157

Kaikkonen, J., T.P. Tuomainen, K. Nyyssönen, J.D. Morrow, and J.T. Salonen. 2004. C18 hydroxy fatty acids as markers of lipid peroxidation ex vivo and in vivo. *Scand. J. Clin. Lab. Invest.* 64:457–468. https://doi.org/10 .1080/00365510410006667

Karagiosis, S.A., and D.F. Ready. 2004. Moesin contributes an essential structural role in *Drosophila* photoreceptor morphogenesis. *Development.* 131:725–732. https://doi.org/10.1242/dev.00976

Krahn, M.P. 2020. Phospholipids of the Plasma Membrane - Regulators or Consequence of Cell Polarity? *Front. Cell Dev. Biol.* 8:277. https://doi.org/ 10.3389/fcell.2020.00277

Kuda, O., M. Brezinova, J. Silhavy, V. Landa, V. Zidek, C. Dodia, F. Kreuchwig, M. Vrbacky, L. Balas, T. Durand, et al. 2018. Nrf2-Mediated Antioxidant Defense and Peroxiredoxin 6 Are Linked to Biosynthesis of Palmitic Acid Ester of 9-Hydroxystearic Acid. *Diabetes.* 67:1190–1199. https://doi .org/10.2337/db17-1087

Kumar, J.P., and D.F. Ready. 1995. Rhodopsin plays an essential structural role in Drosophila photoreceptor development. *Development.* 121:4359–4370.

Laffafian, A., and U. Tepass. 2019. Identification of Genes Required for Apical Protein Trafficking in *Drosophila* Photoreceptor Cells. *G3 (Bethesda).* 9: 4007–4017. https://doi.org/10.1534/g3.119.400635

Lattner, J., W. Leng, E. Knust, M. Brankatschk, and D. Flores-Benitez. 2019. Crumbs organizes the transport machinery by regulating apical levels of PI(4,5)P₂ in *Drosophila*. *eLife.* 8. e50900. https://doi.org/10.7554/eLife .50900

Lee, R.D., C.F. Thomas, R.G. Marietta, and W.S. Stark. 1996. Vitamin A, visual pigments, and visual receptors in *Drosophila*. *Microsc. Res. Tech.* 35: 418–430. https://doi.org/10.1002/(SICI)1097-0029(19961215)35:6<418:: AID-JEMT2>3.0.CO;2-E

Lelli, A., V. Michel, J. Boutet de Monvel, M. Cortese, M. Bosch-Grau, A. Aghaie, I. Perfettini, T. Dupont, P. Avan, A. El-Amraoui, et al. 2016. Class III myosins shape the auditory hair bundles by limiting microvilli and stereocilia growth. *J. Cell Biol.* 212:231–244. https://doi.org/10.1083/ jcb.201509017

Li, B.X., A.K. Satoh, and D.F. Ready. 2007. Myosin V, Rab11, and dRip11 direct apical secretion and cellular morphogenesis in developing *Drosophila* photoreceptors. *J. Cell Biol.* 177:659–669. https://doi.org/10.1083/jcb .200610157

Li, Y., C. Wang, Y. Huang, R. Fu, H. Zheng, Y. Zhu, X. Shi, P.K. Padakanti, Z. Tu, X. Su, et al. 2018. *C. Elegans* Fatty Acid Two-Hydroxylase Regulates Intestinal Homeostasis by Affecting Heptadecenoic Acid Production. *Cell. Physiol. Biochem.* 49:947–960. https://doi.org/10.1159/000493226

Longley, R.L., Jr., and D.F. Ready. 1995. Integrins and the development of three-dimensional structure in the *Drosophila* compound eye. *Dev. Biol.* 171:415–433. https://doi.org/10.1006/dbio.1995.1292

Martin-Belmonte, F., A. Gassama, A. Datta, W. Yu, U. Rescher, V. Gerke, and K. Mostov. 2007. PTEN-mediated apical segregation of phosphoinositides controls epithelial morphogenesis through Cdc42. *Cell.* 128: 383–397. https://doi.org/10.1016/j.cell.2006.11.051

Medelnik, J.P., K. Roensch, S. Okawa, A. Del Sol, O. Chara, L. Mchedlishvili, and E.M. Tanaka. 2018. Signaling-Dependent Control of Apical Membrane Size and Self-Renewal in Rosette-Stage Human Neuroepithelial Stem Cells. *Stem Cell Reports.* 10:1751–1765. https://doi.org/10.1016/j.stemcr.2018.04.018

Missirlis, F., J. Hu, K. Kirby, A.J. Hilliker, T.A. Rouault, and J.P. Phillips. 2003. Compartment-specific protection of iron-sulfur proteins by superoxide dismutase. *J. Biol. Chem.* 278:47365–47369. https://doi.org/10.1074/jbc .M307700200

Morales, F.C., Y. Takahashi, E.L. Kreimann, and M.M. Georgescu. 2004. Ezrin-radixin-moesin (ERM)-binding phosphoprotein 50 organizes ERM proteins at the apical membrane of polarized epithelia. *Proc. Natl. Acad. Sci. USA.* 101:17705–17710. https://doi.org/10.1073/pnas.0407974101

Muñoz, P., K. Fuenzalida, M. Bronfman, A. Gatica, M. Sepúlveda, J. Bacigalupo, A.D. Roth, and R. Delgado. 2013. Fatty acid composition of *Drosophila* photoreceptor light-sensitive microvilli. *Biol. Res.* 46:289–294. https://doi.org/10.4067/S0716-97602013000300010

Muschalik, N., and E. Knust. 2011. Increased levels of the cytoplasmic domain of Crumbs repolarise developing *Drosophila* photoreceptors. *J. Cell Sci.* 124:3715–3725. https://doi.org/10.1242/jcs.091223

Myat, M.M., and D.J. Andrew. 2002. Epithelial tube morphology is determined by the polarized growth and delivery of apical membrane. *Cell.* 111:879–891. https://doi.org/10.1016/S0092-8674(02)01140-6

Nagano, M., K. Takahara, M. Fujimoto, N. Tsutsumi, H. Uchimiya, and M. Kawai-Yamada. 2012. *Arabidopsis* sphingolipid fatty acid 2-hydroxylases (AtFAH1 and AtFAH2) are functionally differentiated in fatty acid 2-hydroxylation and stress responses. *Plant Physiol.* 159:1138–1148. https:// doi.org/10.1104/pp.112.199547

Newsome, T.P., B. Asling, and B.J. Dickson. 2000. Analysis of *Drosophila* photoreceptor axon guidance in eye-specific mosaics. *Development.* 127: 851–860.

Otsuka, Y., T. Satoh, N. Nakayama, R. Inaba, H. Yamashita, and A.K. Satoh. 2019. Parcas is the predominant Rab11-GEF for rhodopsin transport in *Drosophila* photoreceptors. *J. Cell Sci.* 132. jcs231431. https://doi.org/10 .1242/jcs.231431

Ozaki, K., H. Nagatani, M. Ozaki, and F. Tokunaga. 1993. Maturation of major *Drosophila* rhodopsin, ninaE, requires chromophore 3-hydroxyretinal. *Neuron.* 10:1113–1119. https://doi.org/10.1016/0896-6273(93)90059-Z

Pelaseyed, T., and A. Bretscher. 2018. Regulation of actin-based apical structures on epithelial cells. *J. Cell Sci.* 131. jcs221853. https://doi.org/10 .1242/jcs.221853

Pellikka, M., G. Tanentzapf, M. Pinto, C. Smith, C.J. McGlade, D.F. Ready, and U. Tepass. 2002. Crumbs, the *Drosophila* homologue of human CRB1/ RP12, is essential for photoreceptor morphogenesis. *Nature.* 416:143–149. https://doi.org/10.1038/nature721

Pham, H., H. Yu, and F.A. Laski. 2008. Cofilin/ADF is required for retinal elongation and morphogenesis of the *Drosophila* rhabdomere. *Dev. Biol.* 318:82–91. https://doi.org/10.1016/j.ydbio.2008.03.006

Phillips, J.P., J.A. Tainer, E.D. Getzoff, G.L. Boulianne, K. Kirby, and A.J. Hilliker. 1995. Subunit-destabilizing mutations in *Drosophila* copper/ zinc superoxide dismutase: neuropathology and a model of dimer dysequilibrium. *Proc. Natl. Acad. Sci. USA.* 92:8574–8578. https://doi .org/10.1073/pnas.92.19.8574

Pichaud, F., and C. Desplan. 2001. A new visualization approach for identifying mutations that affect differentiation and organization of the Drosophila ommatidia. *Development.* 128:815–826.

Pocha, S.M., A. Shevchenko, and E. Knust. 2011. Crumbs regulates rhodopsin transport by interacting with and stabilizing myosin V. *J. Cell Biol.* 195: 827–838. https://doi.org/10.1083/jcb.201105144

Poole, K., D. Meder, K. Simons, and D. Müller. 2004. The effect of raft lipid depletion on microvilli formation in MDCK cells, visualized by atomic force microscopy. *FEBS Lett.* 565:53–58. https://doi.org/10.1016/j.febslet .2004.03.095

Raghu, P., E. Coessens, M. Manifava, P. Georgiev, T. Pettitt, E. Wood, I. Garcia-Murillas, H. Okkenhaug, D. Trivedi, Q. Zhang, et al. 2009.

Rhabdomere biogenesis in *Drosophila* photoreceptors is acutely sensitive to phosphatidic acid levels. *J. Cell Biol.* 185:129–145. https://doi.org/10.1083/jcb.200807027

Raghu, P., S. Yadav, and N.B. Mallampati. 2012. Lipid signaling in *Drosophila* photoreceptors. *Biochim. Biophys. Acta.* 1821:1154–1165. https://doi.org/10.1016/j.bbalip.2012.03.008

Raghuraman, B.K., S. Hebbar, M. Kumar, H. Moon, I. Henry, E. Knust, and A. Shevchenko. 2020. Absolute Quantification of Proteins in the Eye of *Drosophila melanogaster*. *Proteomics.* doi:10.1002/pmic.201900049. https://doi.org/10.1002/pmic.201900049

Randall, A.S., C.H. Liu, B. Chu, Q. Zhang, S.A. Dongre, M. Juusola, K. Franze, M.J. Wakelam, and R.C. Hardie. 2015. Speed and sensitivity of phototransduction in *Drosophila* depend on degree of saturation of membrane phospholipids. *J. Neurosci.* 35:2731–2746. https://doi.org/10.1523/JNEUROSCI.1150-14.2015

Richardson, E.C., and F. Pichaud. 2010. Crumbs is required to achieve proper organ size control during Drosophila head development. *Development.* 137:641–650. https://doi.org/10.1242/dev.041913

Riga, A., V.G. Castiglioni, and M. Boxem. 2020. New insights into apical-basal polarization in epithelia. *Curr. Opin. Cell Biol.* 62:1–8. https://doi.org/10.1016/j.ceb.2019.07.017

Rodriguez-Boulan, E., and I.G. Macara. 2014. Organization and execution of the epithelial polarity programme. *Nat. Rev. Mol. Cell Biol.* 15:225–242. https://doi.org/10.1038/nrm3775

Sampaio, J.L., M.J. Gerl, C. Klose, C.S. Ejsing, H. Beug, K. Simons, and A. Shevchenko. 2011. Membrane lipidome of an epithelial cell line. *Proc. Natl. Acad. Sci. USA.* 108:1903–1907. https://doi.org/10.1073/pnas.1019267108

Saotome, I., M. Curto, and A.I. McClatchey. 2004. Ezrin is essential for epithelial organization and villus morphogenesis in the developing intestine. *Dev. Cell.* 6:855–864. https://doi.org/10.1016/j.devcel.2004.05.007

Sapp, R.J., J.S. Christianson, L. Maier, K. Studer, and W.S. Stark. 1991. Carotenoid replacement therapy in *Drosophila*: recovery of membrane, opsin and visual pigment. *Exp. Eye Res.* 53:73–79. https://doi.org/10.1016/0014-4835(91)90147-7

Satoh, A., F. Tokunaga, S. Kawamura, and K. Ozaki. 1997. In situ inhibition of vesicle transport and protein processing in the dominant negative Rab1 mutant of *Drosophila*. *J. Cell Sci.* 110:2943–2953.

Satoh, A.K., J.E. O'Tousa, K. Ozaki, and D.F. Ready. 2005. Rab11 mediates post-Golgi trafficking of rhodopsin to the photosensitive apical membrane of *Drosophila* photoreceptors. *Development.* 132:1487–1497. https://doi.org/10.1242/dev.01704

Satoh, A.K., and D.F. Ready. 2005. Arrestin1 mediates light-dependent rhodopsin endocytosis and cell survival. *Curr. Biol.* 15:1722–1733. https://doi.org/10.1016/j.cub.2005.08.064

Satoh, T., A. Ohba, Z. Liu, T. Inagaki, and A.K. Satoh. 2015. dPob/EMC is essential for biosynthesis of rhodopsin and other multi-pass membrane proteins in *Drosophila* photoreceptors. *eLife.* 4. e06306. https://doi.org/10.7554/eLife.06306

Sauvanet, C., J. Wayt, T. Pelaseyed, and A. Bretscher. 2015. Structure, regulation, and functional diversity of microvilli on the apical domain of epithelial cells. *Annu. Rev. Cell Dev. Biol.* 31:593–621. https://doi.org/10.1146/annurev-cellbio-100814-125234

Sawicki, R., S.P. Singh, A.K. Mondal, H. Benes, and P. Zimniak. 2003. Cloning, expression and biochemical characterization of one Epsilon-class (GST-3) and ten Delta-class (GST-1) glutathione S-transferases from Drosophila melanogaster, and identification of additional nine members of the Epsilon class. *Biochem. J.* 370:661–669. https://doi.org/10.1042/bj20021287

Schindelin, J., I. Arganda-Carreras, E. Frise, V. Kaynig, M. Longair, T. Pietzsch, S. Preibisch, C. Rueden, S. Saalfeld, B. Schmid, et al. 2012. Fiji: an open-source platform for biological-image analysis. *Nat. Methods.* 9: 676–682. https://doi.org/10.1038/nmeth.2019

Schopf, K., T.K. Smylla, and A. Huber. 2019. Immunocytochemical Labeling of Rhabdomeric Proteins in *Drosophila* Photoreceptor Cells Is Compromised by a Light-dependent Technical Artifact. *J. Histochem. Cytochem.* 67:745–757. https://doi.org/10.1369/0022155419859870

Schuhmann, K., R. Almeida, M. Baumert, R. Herzog, S.R. Bornstein, and A. Shevchenko. 2012. Shotgun lipidomics on a LTQ Orbitrap mass spectrometer by successive switching between acquisition polarity modes. *J. Mass Spectrom.* 47:96–104. https://doi.org/10.1002/jms.2031

Schuhmann, K., H. Thomas, J.M. Ackerman, K.O. Nagornov, Y.O. Tsybin, and A. Shevchenko. 2017. Intensity-Independent Noise Filtering in FT MS and FT MS/MS Spectra for Shotgun Lipidomics. *Anal. Chem.* 89: 7046–7052. https://doi.org/10.1021/acs.analchem.7b00794

Spannl, S., A. Kumichel, S. Hebbar, K. Kapp, M. Gonzalez-Gaitan, S. Winkler, R. Blawid, G. Jessberger, and E. Knust. 2017. The Crumbs_C isoform of *Drosophila* shows tissue- and stage-specific expression and prevents light-dependent retinal degeneration. *Biol. Open.* 6:165–175. https://doi.org/10.1242/bio.020040

Sykiotis, G.P., and D. Bohmann. 2008. Keap1/Nrf2 signaling regulates oxidative stress tolerance and lifespan in *Drosophila*. *Dev. Cell.* 14:76–85. https://doi.org/10.1016/j.devcel.2007.12.002

Tepass, U., and K.P. Harris. 2007. Adherens junctions in *Drosophila* retinal morphogenesis. *Trends Cell Biol.* 17:26–35. https://doi.org/10.1016/j.tcb.2006.11.006

Walton, K.D., D. Mishkind, M.R. Riddle, C.J. Tabin, and D.L. Gumucio. 2018. Blueprint for an intestinal villus: Species-specific assembly required. *Wiley Interdiscip. Rev. Dev. Biol.* 7. e317. https://doi.org/10.1002/wdev.317

Wodarz, A., F. Grawe, and E. Knust. 1993. CRUMBS is involved in the control of apical protein targeting during *Drosophila* epithelial development. *Mech. Dev.* 44:175–187. https://doi.org/10.1016/0925-4773(93)90066-7

Wodarz, A., U. Hinz, M. Engelbert, and E. Knust. 1995. Expression of crumbs confers apical character on plasma membrane domains of ectodermal epithelia of *Drosophila*. *Cell.* 82:67–76. https://doi.org/10.1016/0092-8674(95)90053-5

Zeidan, Y.H., R.W. Jenkins, and Y.A. Hannun. 2008. Remodeling of cellular cytoskeleton by the acid sphingomyelinase/ceramide pathway. *J. Cell Biol.* 181:335–350. https://doi.org/10.1083/jcb.200705060

Zelhof, A.C., and R.W. Hardy. 2004. WASp is required for the correct temporal morphogenesis of rhabdomere microvilli. *J. Cell Biol.* 164:417–426. https://doi.org/10.1083/jcb.200307048

Zhang, H., N. Abraham, L.A. Khan, D.H. Hall, J.T. Fleming, and V. Göbel. 2011. Apicobasal domain identities of expanding tubular membranes depend on glycosphingolipid biosynthesis. *Nat. Cell Biol.* 13:1189–1201. https://doi.org/10.1038/ncb2328
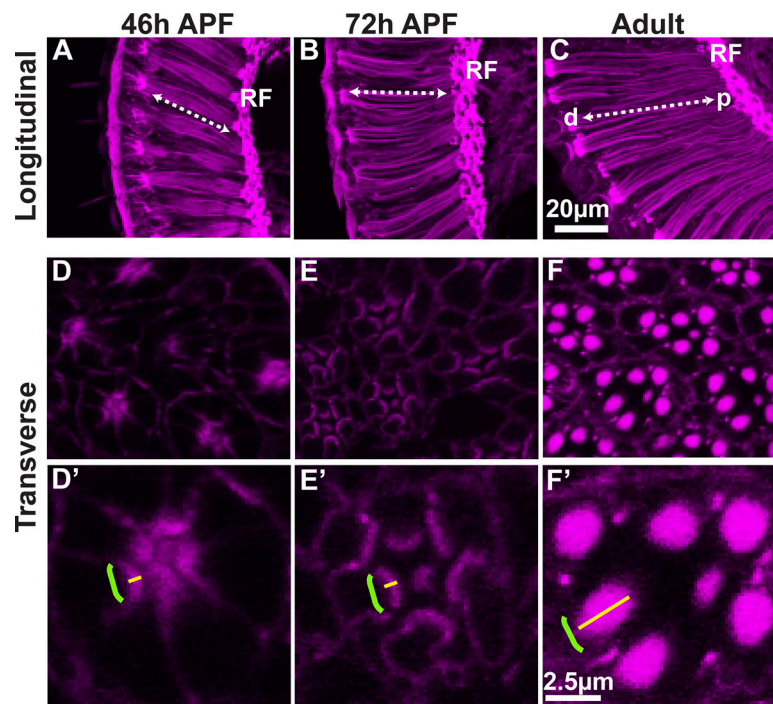
Figure S1. **Growth of rhabdomeres in the last quarter of pupal development is manifested by an extension and an increase in thickness. (A–C)** Projections of confocal stacks obtained from 12-μm-thick longitudinal sections of pupal (A and B) and adult (C) eyes labeled with Alexa Fluor 555-Phalloidin to visualize F-actin. White dashed double-headed arrows indicate the proximodistal axis, with the lens to the left and the retinal floor (RF) to the right. Scale bar is as indicated in C. **(D–F')** Optical sections from 12-μm-thick transverse sections of pupal (D–E') and adult (F and F') eyes, labeled with Alexa Fluor 555-Phalloidin. (D'–F') Individual ommatidia, shown at higher magnification. Yellow solid lines indicate the rhabdomeric thickness along the apicobasal axis of the cell, while the green curved line demarcates the rhabdomere width. Scale bar is as indicated in F'.
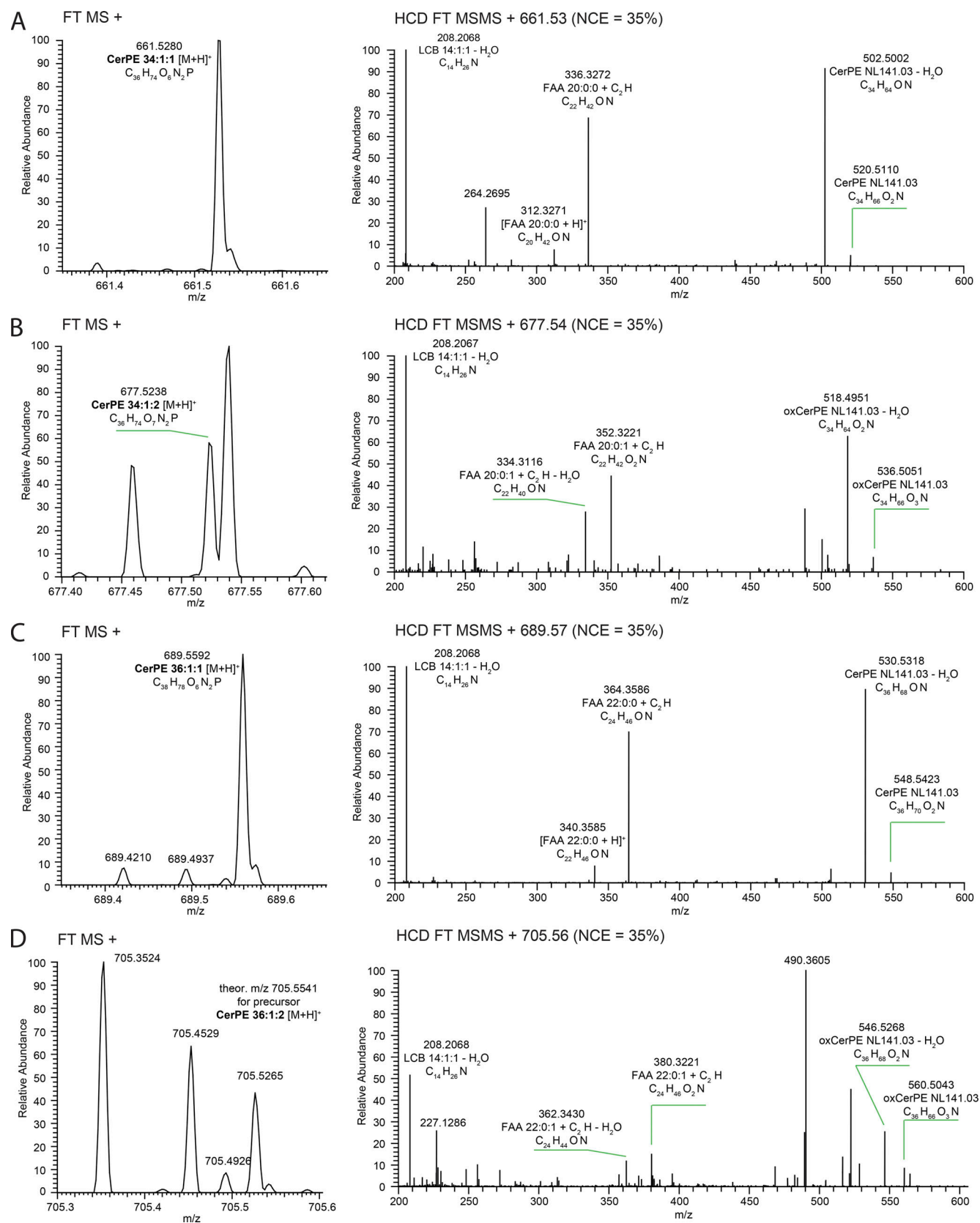
Figure S2. **Identification of CerPE species by FT MS and HCD FT MS/MS in positive ion mode.** Representative FTMS+ (left) and HCD FT MS/MS+ (right) spectra used for the identification of four CerPE species (CerPE34:1:1, A; CerPE 34:1:2, B; CerPE36:1:1, C; and CerPE36:1:2, D). With HCD FT MS/MS, using NCE of 35%, class- and species-specific fragments are obtained; these include species with the neutral loss of m/z 141.03 (CerPE NL), a corresponding water loss (CerPE NL-H₂O), two fatty acid amide (FAA), and the long-chain base fragments (LCB).
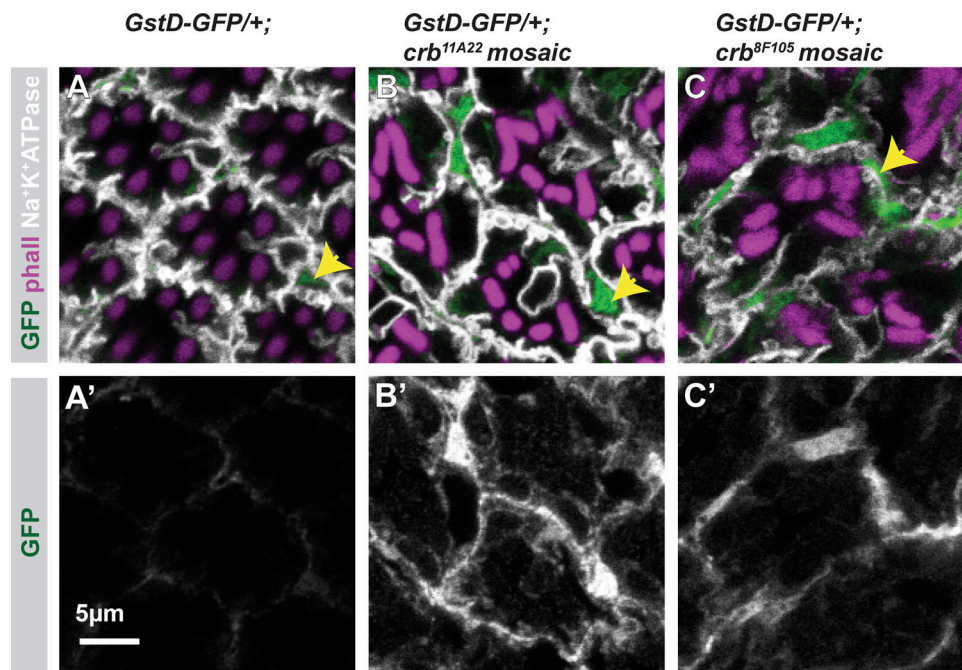
Figure S3.   **Increased intensity of *GstD-GFP* reporter in *crb* mutant PRCs. (A–C')** Optical sections from confocal images of a z-stack of 12-µm transverse cryosections of control (A and A'), *crb*[11A22] (B and B'), and *crb*[8F105] (C and C') mosaic adult eyes carrying a copy of the *GstD-GFP* reporter gene. Tissues are labeled with anti-GFP (green; oxidative stress signaling marker), Phalloidin (phall, magenta) to mark rhabdomeres, and anti-Na⁺-K⁺-ATPase (white) to mark the basolateral membrane of PRCs. A–C are overlay images, whereas A'–C' are the extracted grayscale images of the *GstD-GFP* channel. The GFP signal in control is detected in the tertiary pigment cells (yellow arrow) but cannot be detected in PRCs (A'). In mutant ommatidia, the GFP signal not only is increased in pigment cells (yellow arrows), but also is detected in PRCs (B'–C') as indicated by the signal within the hexagonal outline of the ommatidium.
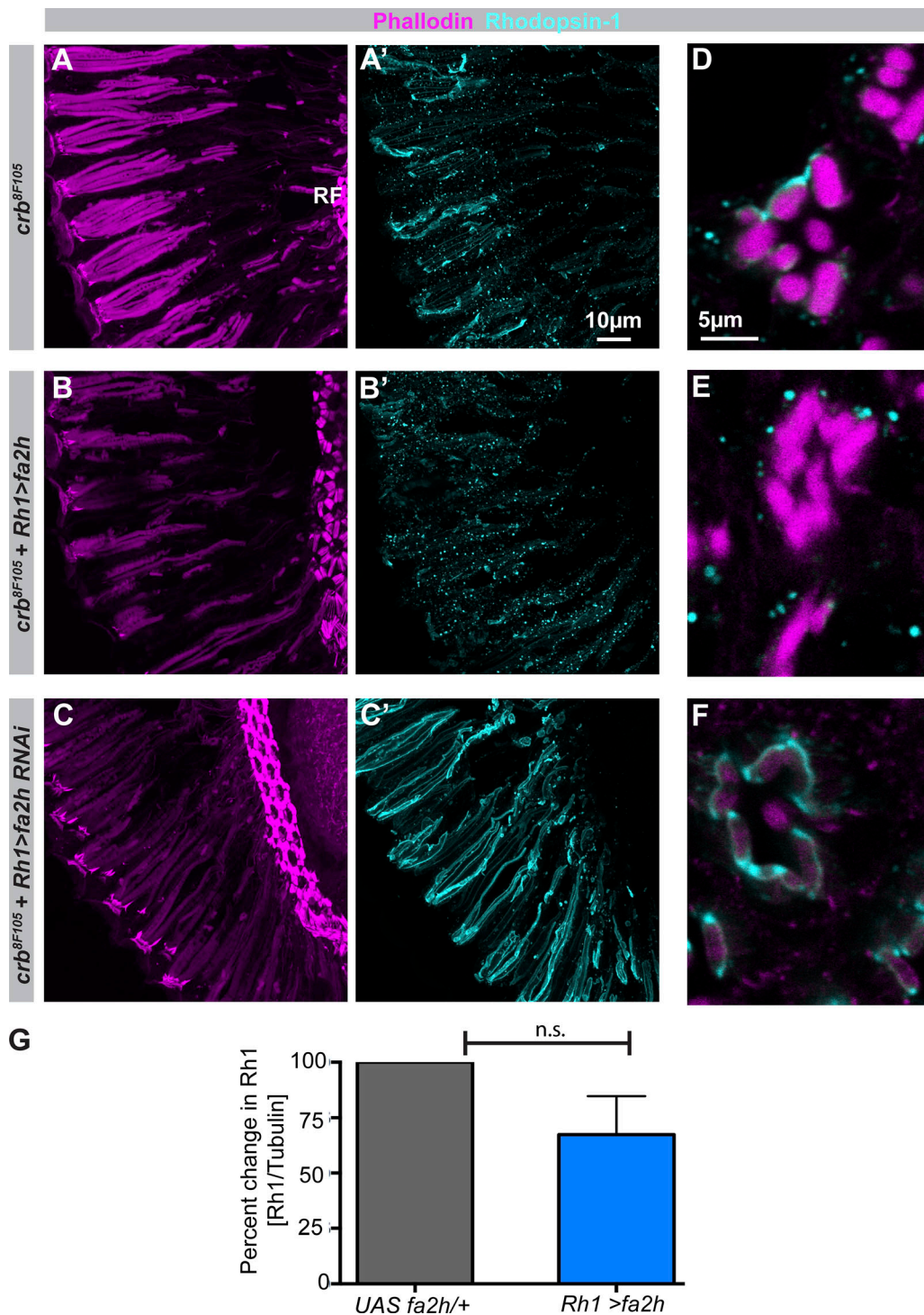
Figure S4. Rh1 localization at steady state. (A–F) Projections of confocal stacks obtained from 12-µm horizontal sections (A–C') and 1-µm optical sections from 12-µm cross sections (D–F) of adult fly heads of indicated genotypes, labeled with Alexa Fluor 555-Phalloidin (magenta), to visualize F-actin, and an antibody against Rh1 (cyan). Note increased cytoplasmic, Rh1-positive punctae upon *fa2h* overexpression (B' and E) and more rhabdomeric Rh1 staining upon knocking down *fa2h* (C' and F) in a mutant background. **(G)** Graph representing percentage change of normalized Rh1 levels (mean ± SEM) in adult heads, following normalization to loading control Tubulin, obtained from Western blots of controls (*UAS fa2h/+*; gray) and upon *fa2h* overexpression (*Rh1>fa2h*; blue). Sample size = five independent biological replicates of five heads each.
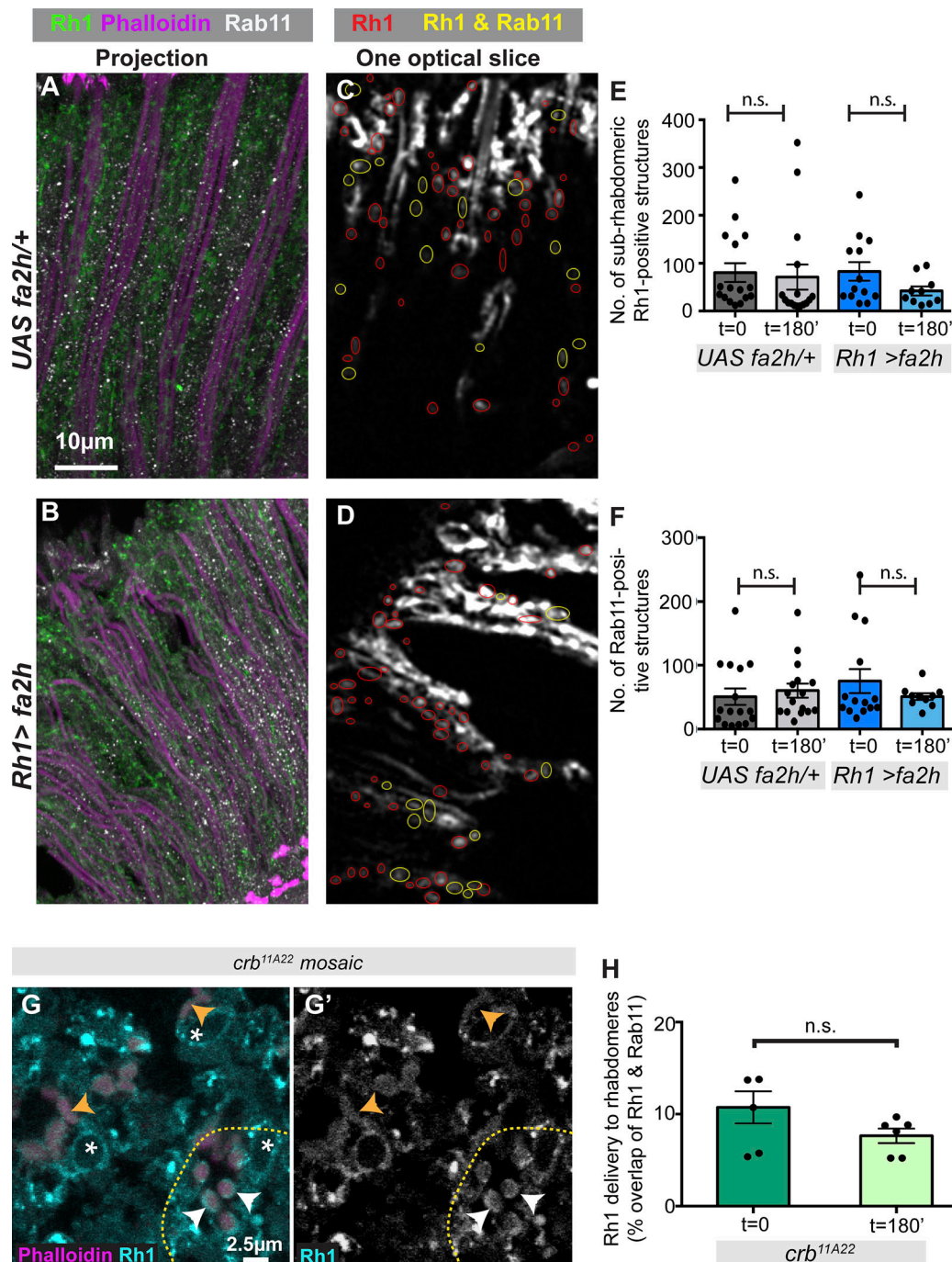
Figure S5. **Rh1-Rab11 overlap following BLICS assays. (A–D)** A and B are projected overlays of 12-μm sections of fly eyes labeled with phalloidin and antibodies against Rh1 and Rab11 following 180 min of BLICS. C and D are representative optical slices from the projections shown in A and B, respectively, after application of the ComDet plugin for quantification. Red outlines are the Rh1-positive structures outside the rhabdomere (not overlapping with phalloidin staining), whereas yellow outlines are a subset of these Rh1-positive structures that overlap with Rab11-positive structures. **(E and F)** Graphs representing the number (no.) of sub-rhabdomeric Rh1-positive (E) and Rab1l-positive (F) structures along the rhabdomere length, obtained from BLICS assays ($t = 0$ and 180 min after blue light exposure and with retinal supplementation) in control (gray) and upon *fa2h* overexpression (blue). The number of structures is estimated from confocal images of fly eye sections labeled with antibodies against Rh1 and Rab11. **(G)** Image showing a single optical cross section of a mosaic *crb11A22* adult eye double labeled with Alexa Fluor 555-Phalloidin (magenta) and an antibody against Rh1 (cyan) at $t = 180$ min (180') after blue light exposure and with retinal supplementation. **(G')** Extracted Rh1 channel in grayscale of the image shown in G. Yellow dashed line demarcates the wild-type and mutant clones. BLICS assays reveal that in wild-type photoreceptor cells at this time point, Rh1 is visible in the perinuclear ER (white asterisk) and as a crescent staining in the rhabdomere (white arrowhead). However, in mutant rhabdomeres, easily identified by their abnormal morphology (orange arrowheads), less Rh1 is detected in the rhabdomere. Scale bar is as indicated in G. **(H)** Graph representing percent overlap (mean ± SEM) of sub-rhabdomeric Rh1- and Rab11-positive structures, along the rhabdomere length, obtained by BLICS assays ($t = 0$ and 180 min after blue light exposure and with retinal supplementation) in mosaic *crb11A22* adult eyes. In mutant PRCs, no difference in extent of overlap between Rh1 and Rab11 following BLICS is observed, implying a restriction on delivery of Rh1 to the rhabdomeres.

Hebbar et al.
Hydroxylated sphingolipids in apical domain growth

Journal of Cell Biology   S5
https://doi.org/10.1083/jcb.201911100

Provided online are five tables. Table S1 describes fly lines. Table S2 lists genotypes. Table S3 lists chemical reagents and antibodies. Table S4 lists primers. Table S5 lists abbreviations. Data S1 contains the lipid species abundance (as mol%) across different alleles and controls (for each condition, there are at least n = 3 biological replicates) used in this study.